Resistive switching with chalcogenide thin layer

By

Bo Zhang

Supervisor: Prof. Ing. Tomáš Wágner

A Dissertation Submitted to the Faculty of Chemical Technology

Department of General and Inorganic Chemistry

In Partial Fulfilment of the Requirements

For the Degree of

DOCTOR OF PHILOSOPHY

UNIVERSITY OF PARDUBICE

2017

ACKNOWLEDGMENTS

Contents

LIST OF FIGURES

LIST OF TABLES

Keywords:

Resistive switching, chalcogenide thin layer, conductive filament

Abbreviations:

DRAM: dynamic random access memory

ROM: read only memory

RAM: random access memory

FRAM: ferroelectric random access memory

PRAM: phase change random access memory

MRAM: magnetoresistive random access memory

AFM: atomic force microscope

OIDD: optical induced diffusion and diffusion

SEM: scanning Electron Microscope

RRAM: resistive random access memory

CBRAM: conductive bridge memory

PVD: physical vapor deposition

PECVD: plasma-enhanced chemical vapor deposition

AAO: anodic aluminum oxide

GST: germanium-antimony-tellurium

RF: radio frequency

RS: resistive switching

PLD: pulsed laser deposition

ALD: atomic layer deposition

UV: ultraviolet

AIDCN: 2 - amino - 4, 5 - imidazoledicarbonitrile

TCNQ: 7, 7, 8, 8 - tetracyanoquinodimethane

NPB: N, N' - Bis (naphthalen - 1 - yl) - N, N' - bis (phenyl) benzidine

Rose bengal: 4, 5, 6, 7 - Tetrachloro - 2' , 4 ', 5 ', 7 ' - tetraiodofluorescein disodium salt

MEH - PPV: poly [2 - methoxy - 5 - (2 - ethylhexyloxy) - 1, 4 - phenylenevinylene]

P3HT: poly (3 - hexylthiophene - 2, 5 - diyl)

PARA: poly (o - anthranilic acid)

Parylene - C: poly - p - xylene

PEDOT: PSS: poly (3, 4 - ethylenedioxythiophene) polystyrene sulfonate

PFN - C: poly [(9, 9 - bis (3ethylenedioxythiophene) polystyrene sulfonatet - 2, 7 - (9, 93ethylenedioxythio]

PFO: polyfluorene

PI: polyimide

PMMA: poly (methyl methacrylate)

PS: polystyrene

PVA: poly (vinyl alcohol)

PVK: poly (9 - vinylcarbazole)

PVP: poly vinyl pyrrolidone

WPF - oxy - F: poly[(9, 9 - bis((6 ' - (N, N, N - trimethylammonium) hexyl) - 2 , 7 - fluorene) - alt - (9, 9 - bis(2 - (2 - methoxyethoxy) ethyl) - fluorene)] dibromide

LSMO: lanthanum strontium manganite

PCMO: $Pr_{1-x}Ca_xMnO_3$

1T1R: one - transistor one - resistor

1D1R: one - diode one - resistive switching memory

1BJT1R: one - bipolar junction transistor one - resistive switching

Abstract

Resistive switching memory technology shows promising future to replace the traditional flash-disc or disk memory. Ag or Cu doped chalcogenide thin layer is typical electrolyte and the high and the low resistance is adjusted due to the formation and dissolution of conductive filament. More specifically, AsS_2 and $GeSe_2$ were selected as electrolyte and Ag was doped in the electrolyte layer by photo doping and dissolution from the top or bottom of electrolyte layer. In addition, the geometries of device also influence the parameters of resistive switching behaviour. Therefore, five different geometries were discussed in the context and the electrodes sizes ranges form from 1 mm to 5µm. In order to obtain graphic electrode with various size, stencil mask and photoresist lithography was applied to the sample.

I-V test was done by DC sweep mode, which the threshold of SET bias can be obtained. The scanning electron microscope and atomic force microscope were utilized to locate the filament and characterize the outline of filament. The conductive atomic force microscope was only used to characterize the distribution of conductive region, which equals to the distribution of filament. As Ag doped chalcogenide thin layer is vulnerable to electron beam, the observation of filament was accomplished by scanning electron microscope and outline of the filament is clear.

1 Introduction

With the development of microelectronic devices, Information technology becomes one of the most important areas. John von Neumann pointed out the basic five parts of computer: Input Unit, Output Unit, Storage Unit, Central Processing Unit and Control Unit, in which the memory device belongs to the storage unit [1]. Two basic states are adopted for data storage, which is "1" and "0" in binary code. Based on the different mechanisms, the memory devices can be divided into two parts: volatile and nonvolatile memories. The volatile memory cannot save data without the power supply. Therefore, it is only used for short term data storage, for instance dynamic random access memory (DRAM) [2]. In contrary, the nonvolatile memory is capable of maintaining the data with or without the power supply, for instance flash disks. Based on the method of reading and writing data, the memory devices can also be attributed into two categories: read only memory (ROM) and random access memory (RAM). ROM is only for reading. Whereas RAM can be used for both reading and writing [3]. Nowadays, many different approaches have been employed for data storage. Researchers focused on several special material fabricated device, such as ferroelectric RAM (FRAM) [4], phase

change RAM (PRAM) [5], magnetoresistive RAM (MRAM) [6] and resistive switching RAM (RRAM) [5].

Resistive switching relays on the reversible resistance change of the medium layer, realizing the data memory. The advantages such as fast response speed, low energy consumption, long-time data storage, long term usage of resist and the semiconductor process compatibility makes the RRAM memories a promising next generation of data memories [5]. The scope of resistive switching comprises the microelectronics, materials, physics and chemistry, thus, it is a new interdisciplinary field [7]. However, the detailed mechanism of switching is still unclear [8]. According to the switching behaviour of resistive switching, the RRAM can be described as two types: unipolar and bipolar. The unipolar resistive switching relies on the amplitude of applied bias with the polarity, and bipolar switching relies on the amplitude and the polarity of applied bias [9]. From the materials in PRAM point of view, oxide and chalcogenide thin layers are dominant. The conductive filament can be either metallic filament or oxygen vacancy filament in oxide layer, compared with only metallic filament in chalcogenide thin layer [10]. The main aim of this thesis is discussion of the switching behavior and observation of filaments in chalcogenide layers.

The Ag or Cu doped chalcogenide electrolyte is mostly fast ion conductor. The memory device usually comprises an inert electrode, a diffusive Ag or Cu electrode and a chalcogenide electrolyte layer in-between. The mechanism of filament formation involves the reduction-oxidation reactions of ions leading to the formation or dissolution of metallic filaments [11]. Such memory cell is referred as programmable metallization cell (PMC) [12] or conductive bridging RAM (CBRAM) [13] . PMC cell owns excellent storage performance, for instance, low operative voltage, low operative current, fast response and long-time data storage. In 2005, Terabe *et al.* [14] reported the atomic switching in $Ag/Ag_2S/Pt$ structure showing potential application in logic gate, which is promising to be applied in computer science.

In this thesis, five different geometries of switching devices are presented: spot geometry, crossbar geometry, needle contact geometry, tip (conductive AFM) geometry and via-hole geometry (See the section "graphic illustration of sample preparation"). Each of these geometries has different advantages and drawbacks and offers alternative view to understand the switching mechanism. More importantly, the scanning electron microscope and atomic force microscope images partially exhibit the outline of conductive filament, providing solid evidence for filament study.

2 The principle material in resistive switching

2.1 Material selection

The first experimental observation of resistive switching can be dated back to more than half a century ago. The first observation of conductive filament was done in 1976 in Ag/Ag-As$_2$S$_3$/Au device (Figure 1) [15].
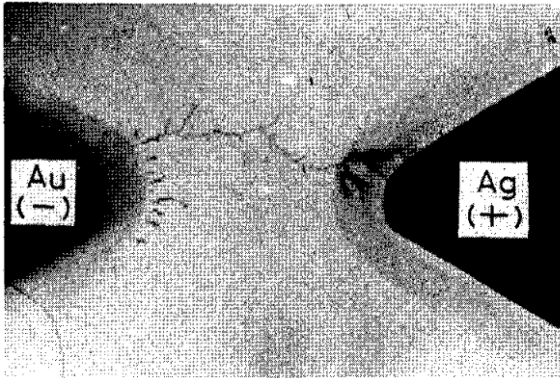
Figure 1: The Ag dendrite bridge [15].

The urgency to find the appropriate alternative to/for flash memory increases the demand for searching the resistive switching electrolyte material, especially in the past few decades. The list of resistive switching materials is presented in Table 1 [16]. One can observe a large number of high-k materials exhibiting the resistive switching, which can be categorized into chalcogenides, oxides (binary, ternary and more complex), nitrides, amorphous silicon, and some organic materials with flexible substrate. Among these materials, binary oxides have been extensively investigated due to their relatively good compatibility during the fabrication process (photoresist lithography, etc.) and desirable reproducibility [16].

Table 1: List of electrolyte materials for resistive switching [16].

Binary oxides			Chalcogenides		
MgO$_x$	Unipolar	Bipolar	Cu$_2$S	Bipolar	
AlO$_x$	Unipolar	Bipolar	GeS$_x$	Bipolar	
SiO$_x$	Unipolar	Bipolar	Ag$_2$S	Bipolar	
TiO$_x$	Unipolar	Bipolar	GeSe$_x$	Bipolar	
CrO$_x$	Bipolar		**Nitrides**		
MnO$_x$	Unipolar	Bipolar	AlN	Unipolar	Bipolar
FeO$_x$	Bipolar		SiN	Unipolar	Bipolar
CoO$_x$	Unipolar	Bipolar	**Small molecules**		
NiO$_x$	Unipolar	Bipolar	AIDCN	Bipolar	
CuO$_x$	Unipolar	Bipolar	AlQ$_3$	Unipolar	Bipolar
ZnO$_x$	Unipolar	Bipolar	Cu:TCNQ	Bipolar	
GaO$_x$	Bipolar		NPB	Bipolar	
GeO$_x$	Unipolar	Bipolar	Rose bengal	Bipolar	
ZrO$_x$	Unipolar	Bipolar	**Polymers**		
NbO$_x$	Unipolar	Bipolar	MEH-PPV	Unipolar	Bipolar
MoO$_x$	Unipolar	Bipolar	P3HT	Unipolar	Bipolar
HfO$_x$	Unipolar	Bipolar	PARA	Unipolar	Bipolar
TaO$_x$	Unipolar	Bipolar	Parylene-C	Bipolar	
WO$_x$	Unipolar	Bipolar	PEDOT:PSS	Unipolar	Bipolar

CeO$_x$	Unipolar	Bipolar	PFN-C	Unipolar	
GdO$_x$	Unipolar	Bipolar	PFO	Unipolar	
YbO$_x$	Unipolar	Bipolar	PI	Unipolar	Bipolar
LuO$_x$	Unipolar	Bipolar	PMMA	Bipolar	
Ternary or quaternary oxides			PS	Unipolar	Bipolar
LaAlO$_3$	Bipolar		PVA	Bipolar	
SrTiO$_3$	Bipolar		PVK	Unipolar	Bipolar
BaTiO$_3$	Unipolar	Bipolar	PVP	Bipolar	
LC(or S)MO	Bipolar		WPF-oxy-F	Bipolar	
PCMO	Bipolar		**Others**		
BiFeO$_3$	Unipolar	Bipolar	Graphene oxide	Bipolar	

Ionic conductivity occurs in liquid electrolytes, crystalline and amorphous solids. While in liquids, the conductivity is contributed from both anions and cations. In solid electrolytes, only cations or anions can move, and the conjugate species are fixed into lattice positions. Ions can move inside a solid, if sites are available for them. The reason for higher ionic conductivity in amorphous material might be related to the low density and flexible structure containing more free volume, through which ions can move freely [17]. The basic movement is described as a sequence of discrete jumps of an ion from an occupied site to a near unoccupied one through an energy barrier. In order for ions to move through a solid, they must possess a sufficient energy to overcome the energy barrier. Further, an equivalent lattice site next to a given ion must be empty in order to occupy by ion. Cationic conductors are also known as "superionic" or "fast ion" conductors [18].

The common used resistive switching electrolyte material is Ag or Cu doped chalcogenide thin layer, with inert and diffusive electrode, referred as PMC (programmable metallization

cell) or CBRAM (conductive bridging RAM) [19]. Figure 2 schematically shows the basic principle of the resistive switching [20]. The setup for electrochemical metallization memory cells is very similar to the electrochemical cells with a liquid electrolyte, where the conductive filaments are formed in a solid electrolyte [21]. In electrochemical metallization cells, the solid electrolyte is sandwiched between an inert, e.g. Pt or W, and a diffusive, e.g. Ag or Cu, electrode (Figure 2(a)). At least two stable states are expressed by the formation and dissolution of a metallic filament between the electrodes. Under application of a positive bias to the diffusive electrode, diffusive electrode is oxidized into ions which migrate through the solid electrolyte. These ions are reduced at the inert electrode, where they form an electrodeposited filaments [22]. When the filament reaches the diffusive electrode, the initially highly resistance of cell switches to a low resistance state (ON state after SET process) due to a short circuit between top and bottom electrode (shown in Figure 2(a) II.). Under reverse bias the filament is electrochemically dissolved and the cell is switched back to the high resistance state (OFF state after RESET process) (shown in Figure 2(a) III. and IV.). The memory state can be kept without external electric supply, which is known as non-volatile state.
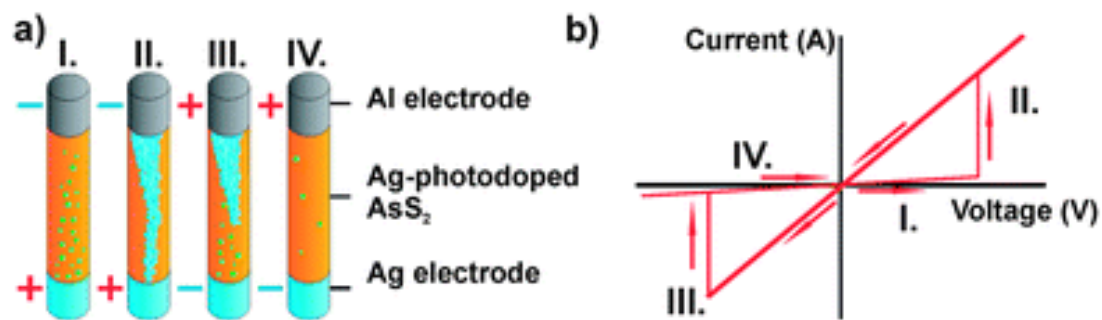
Figure 2: Resistive switching cell (a) the scheme of operation, symbols "+" and "−"show the plus and negative polarity, (b) the I-V curve of resistive switching with 4 different stages [20].

Various materials are known to allow metal ion migration and filament formation and filament rupture [23]. Resistive switching based on metal filament formation and its rupture is also shown in Ag_2S [24] and Cu_2S [25]. In this context, especially Cu-doped SiO_2 is an interesting material combination, because Cu as well as SiO_2 arwe already present in standard semiconductor processes. Therefore, memory cells based on these materials will allow for an easy integration into current semiconductor process lines [15].

Oxide can also form conductive filament via oxygen vacancies. Most of binary and complex oxides can form oxygen vacancies, for instance TiO_x, HfO_x. Due to the migration of oxygen vacancies, the conductive filament is able to form at the defect positon or it might be possible to form low valence state oxide filament [26].

2.2 Algorithm of measurement

Depending on the type of resistive switching, the measuring algorithm can be different. Under appropriate current or voltage application, various materials show a change in resistance, but the switching mechanisms are different. Two main switching schemes can be distinguished as polarity dependent bipolar switching and polarity independent unipolar switching, as shown in Figure 3.
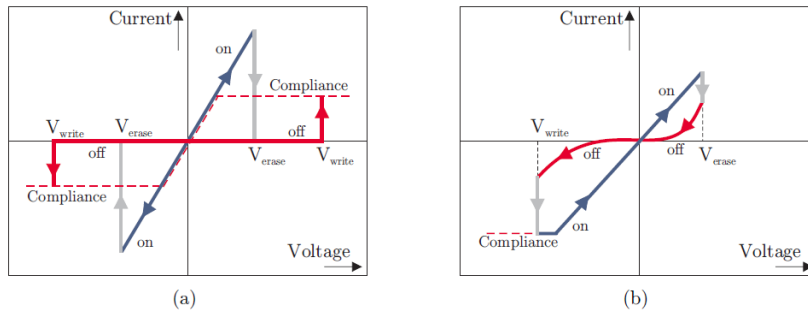
Figure 3: Switching scheme (a) unipolar switching, (b) bipolar switching [19].

In case of unipolar resistive switching, switching to the low resistance (ON) state, i.e. writing the cell, occurs under the same voltage polarity as switching to the high resistance (OFF) state, i.e. erasing the cell. Mostly, the absolute value of the voltage for writing, V_{write}, is higher than the voltage for erasing, V_{erase}. Unipolar switching is schematically shown in Figure 3 (a). There exist some models, for instance 'Thermal Dissolution Model', which can be used to explain the phenomena. In most of the cases, it is understood as a thermal assisted process. A current compliance during writing is typically used to control the low resistance state [8]. Typical device of unipolar cell is shown in Figure 4. The conductive AFM (C-AFM) shows the conductive channel before and after RESET process. The current density decreased after RESET process, indicating the fracture of filament [27].
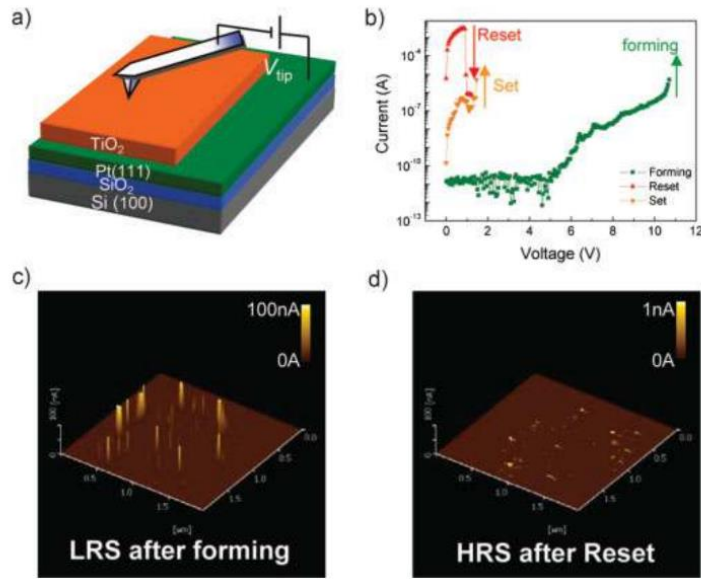
Figure 4: AFM measurements. (a) Schematic diagram of the C-AFM measurements. (b) I-V curves using the conducting AFM tip as a top electrode, clearly show the forming, RESET, and SET operations. As all biases are in the same polarity, this is a unipolar switching. (c) Mapping of the current flow through the surface right after the forming operation with $V_{tip} = 8$ V shows locally distributed conducting regions. (d) After the RESET operation with applied bias 1 V, the current in conductive channel decreased [27].

In case of bipolar switching, writing and erasing occur under different polarities. A typical bipolar current-voltage characteristic is shown in Figure 3 (b). The bipolar switching device shows a notable different asymmetry structure from unipolar switching device. The asymmetry structure consists of inert and diffusive electrode. Electroforming is typically the first switching cycle, which is an electric breakdown of memory cell to the low resistance state. In addition, the electroforming voltage is commonly larger than the following SET voltage.

2.3   Mechanism of resistive switching

The model of metallic conductive filaments is created for explaining the resistive switching phenomena in fast ion conductor, which is called electrochemical metallization, conductive bridging cell, or programmable metallization. Resistive switching in chalcogenide materials doped with Ag or Cu has been explained by this model, as described in previous chapter.

The resistive switching in chalcogenide relies on the redox reaction and migration of cations (Ag^+, Cu^{2+}). There is another type of resistive switching in oxide devices working with migration of anions, which involves the oxygen vacancies. Such devices consist of an inert

electrode, for instance Pt or Au and a relatively active electrode, for instance Al, Ti Ta, or Nb. However, neither electrode is able to induce formation of the metal conductive filament, in contrast to Ag or Cu electrode. In general, during the first switching cycle, an electroforming process is needed to 'SET' the low resistance state, in which enough oxygen vacancies are produced under bias, in order to guarantee the following switching process. In this process, oxygen gas is emitted, sometimes forming bubbles on the topmost of thin layer. The typical device is $Pt/TiO_2/Pt$, as shown in Figure 5 [28].
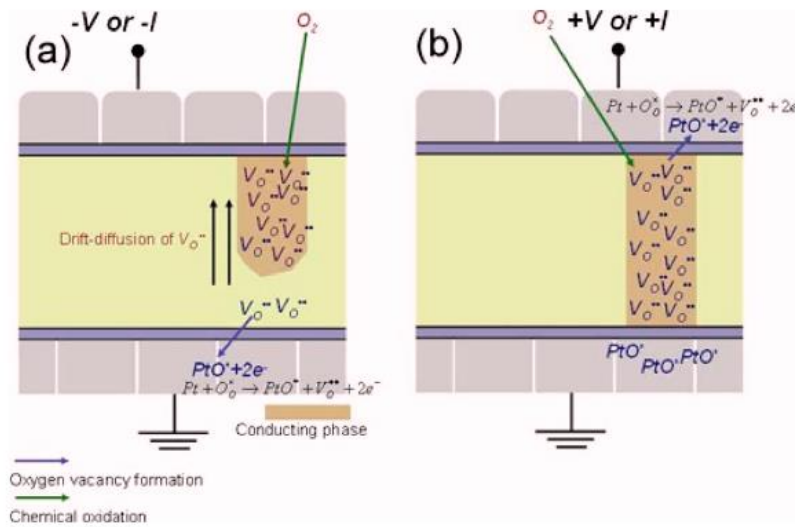
Figure 5: Schematic sketches of electroforming of conductive filament in air. The geometry of a conducting phase resulted from (a) applied positive bias, (b) applied negative bias [28].

As described above, the electroforming process produces oxygen gas, causing the morphology change of topmost electrode. Yang *et al*. [29] studied the morphology variation in $Pt/TiO_2/Pt$ device, proving the existence of oxygen ion exchange at the interface. As shown in Figure 6, during switching process, it can be observed the appearance of air bubbles under −4 V (Figure 6 (a) and (b)) and remained without applied bias (c). Under +4 V, more bubbles emerged (Figure 6 (d) and (e)). After the test, all bubbles disappeared (Figure 6 (f)). AFM images show the permanent deformation of electrode after the switching process (Figure 6 (g)). Figure 6 (h) depicts the creation of air bubbles under large bias. All the images prove that migration and electrochemistry reaction determine the resistive switching in $Pt/TiO_2/Pt$ device [29].
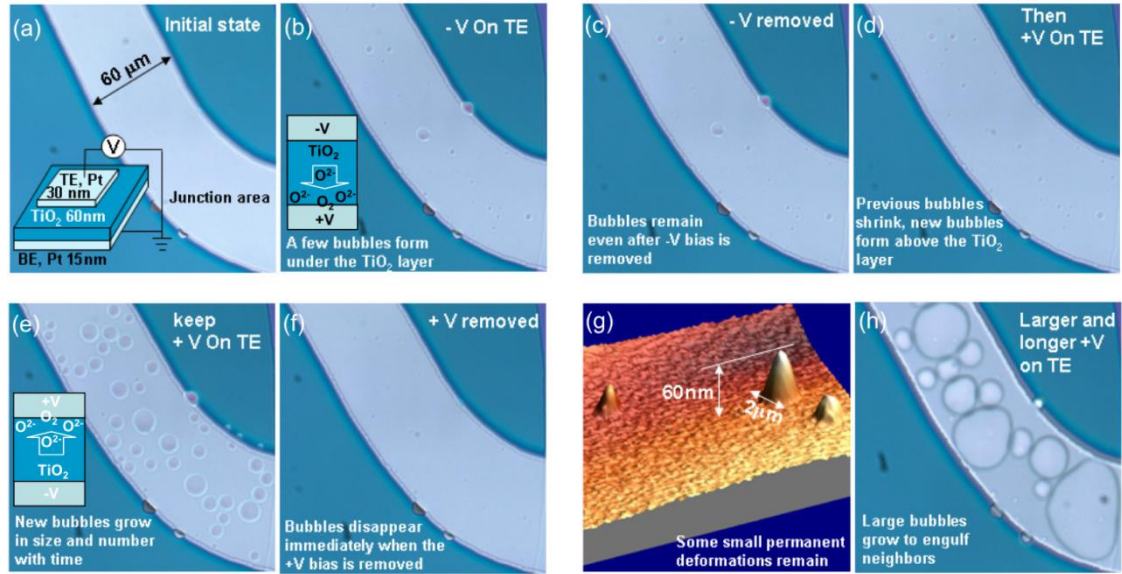
Figure 6: The dynamic images of air bubbles in Pt/TiO$_2$/Pt cell [29].

Besides bipolar resistive switching, unipolar switching devices are mostly prepared with oxide thin layer, which the conductive filament mainly consists of oxygen vacancy or defects. In such devices, the joule heat is the main driving force for dissolution of conductive filament. Commonly, such device consists of a symmetric structure, for instance Pt/NiO/Pt [30], Pt/CoO/Pt [31] and Pt/ZnO/Pt [32]. During resistive switching process, a current limit is set to avoid the breakdown of device. However, a large current is needed in RESET process, as it is described in Figure 3 (a).

2.4 Chalcogenide glasses

Chalcogenide glasses consist of the chalcogenide elements S, Se, and Te alloyed together with other elements such as Ge, As, Sb, Ga, etc. [33]. We can classify the amorphous chalcogenide into the elemental (S, Se, Te), binary (As$_2$S$_3$, As$_2$Se$_3$, etc.), ternary and more complicated (As-S-Se, Ge-Sb-Te, etc.) systems and the alloys can be divided into stoichiometric (As$_2$S$_3$, GeSe$_2$) and non-stoichiometric compositions (S–Se, As–Se) [34].

Chalcogenide bulk glasses are prepared by quenching of the corresponding melt. The composition of bulk is prepared by weighing of the elements in required concentrations and then sealing them in quartz ampoules under high vacuum. The sealed ampoules are kept in a rocking furnace at a temperature to keep the melt homogeneous. Fast cooling is done in iced water, liquid nitrogen or even in the air depending upon the required cooling rate. The glass

formation depends on many of factors, e.g. kinetic, structural and chemical factors. Some of the materials can be made in glassy form at the faster cooling rates, for instance splat cooling.

The chalcogenide thin layers can be prepared by physical vapor deposition (PVD) method such as thermal evaporation, flash thermal evaporation or sputtering. PVD: Thermal evaporation is common for the simple compositions, such as pure Se. The evaporation of chalcogenide compounds depends more on the kind of materials, for example As_2S_3 is more suitable for slow evaporation and GeS_2 can only be prepared by sublimation methods. Flash evaporation technique is similar to thermal evaporation, except that the material is dropped on a filament or boat which has been heated. Thus, allows the deposition of more complex materials than common thermal evaporation. Sputtering Technique: Sputtering is based on bombardment of a target material by the energetic ions from low-pressure plasma, causing erosion of material, either atom by atom or as clusters of atoms, and subsequently deposition of layer on the substrates. Simplest way to induce sputtering is to apply a high negative voltage to the target surface, thereby attracting positive ions from the plasma. However, DC sputtering process is feasible only when target is sufficiently conductive [35].

2.5 Photo and thermal diffusion

Ag^+ or Cu^{2+} ions can be introduced into the chalcogenide material by various methods, for instance by evaporation, co-sputtering, photo diffusion, thermal diffusion, and by pulsed laser deposition.

Photo diffusion or doping was found by Kostyshin *et al*. [36] and mostly used for Ag doping. The Ag profile of Ag/AsS_2 bilayer is in a step shape with a concentration of 25% (i.e. $AgAsS_2$), as shown in Figure 7. Accordingly, the structure gradually changes from Ag/AsS_2 to $Ag/AgAsS_2/AsS_2$ during photo dissolution of Ag in AsS_2 [37].
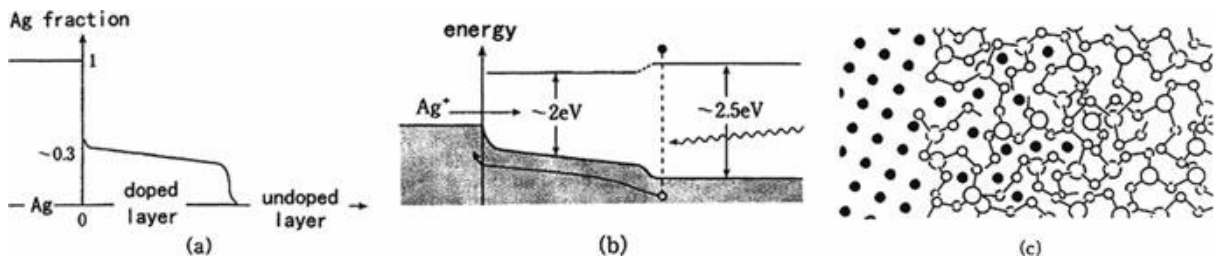
Figure 7: Schematic illustration of composition profile in ($Ag/AgAsS_2/AsS_2$) after photo doping. (a) Ag concentration profile, (b) band diagram, and (c) schematic atomic structure, in which the black circles are Ag atoms, the big open circles are As atoms, and the small open circles are S atoms [37].

Experiments suggest the dissolution of Ag ion into chalcogenide thin layer is closely related with the flow of holes. From the thermodynamic aspect, it can be found an interesting region with free energy minimum where the composition near of $AgAsS_2$ corresponds to the glass forming region in Ag-As-S system, which displays minimum energy in the Figure 8 [38].
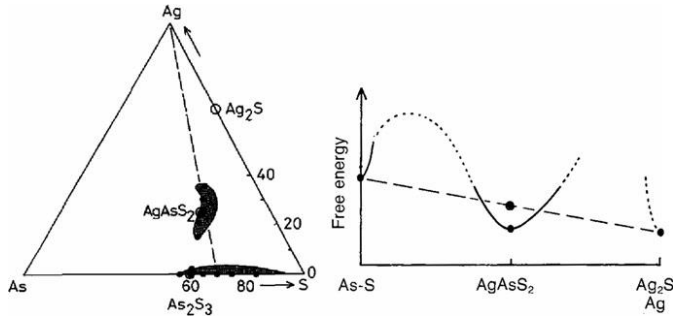
Figure 8: Glass-forming regions of Ag–As–S system (left) and estimated free energy curve along As–S and Ag–S lines (right) [38].

2.6   Photo-surface deposition

Photo-surface deposition is the opposite phenomena against the photo doping effect, which was found by Maruno and Kawaguchi [39]. In short, it is a segregation of Ag particles on the surface of the chalcogenide thin layer, due to the exposure of illumination. The mechanisms of the photo-surface deposition can be understood as follows: the counter flow of Ag^+ ions and holes is resulted in forming the glass composition (Ag_xAsS_2, x>1). The photo-electronic force tends to separate Ag from $AgAsS_2$ (Figure 9) [40].
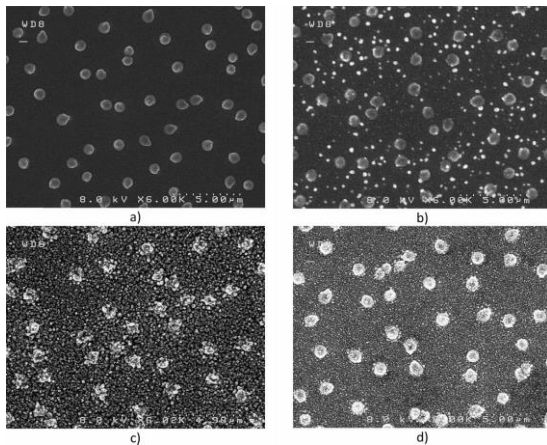
Figure 9: SEM images of radiation-induced Ag surface deposition at various radiation doses: (a) 1.58 Mrad, (b) 3.19 Mrad, (c) 7.59 Mrad, and (d) 14.82 Mrad [40].

2.7 Application of chalcogenide glass in resistive switching

In 1976, Hirose *et al*. [15] found the first Ag/Ag-As_2S_3/Au resistive switching device, and observed the filament. Terabe *et al*. [14] announced a quantized conductance atomic switch, based on Ag/Ag_2S/Pt structure. The mechanism is based on the formation and dissolution of Ag atom bridge (Figure 10). In 2007, Dietrich *et al*. [41] published a test of 2 Mbit microchip made by Ag-doped chalcogenide thin layer. However, chalcogenide thin layers are not, so far, compatible with the present microelectronic technology, in which it could compete with metal-doped oxide thin layers, e.g. by WO_x or SiO_2 [42].
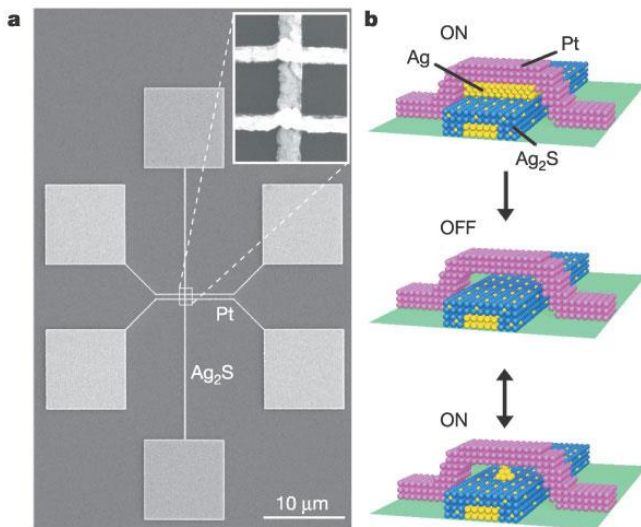
Figure 10: The basic structure of memory cell and Ag atom bridge [42].

In detail, the binary sulphide and selenide compounds are the most common chalcogenide materials. The device structure is the same as discussed above. In binary sulphide thin layers, for instance GeS_2 and As_2S_3, the Ag ions are doped by photo doping in an inert environment and Cu ions are introduced into thin layer by thermal doping. Ag^+ ions are more mobile than Cu^{2+} ions. Cu^{2+} ions show the tendency to strength the network connectivity of glass [43]. In binary selenide thin layer e.g. $GeSe_2$, Ag photodissolution is very fast, due to thermally activated diffusion of Ag^+ ions [44]. Therefore, a resistive barrier of device or a pre-set electroforming process should be preformed before switching. In order to eliminate an extra loss of active metal electrode, oxide thin layer is typically used for selenide thin layer, for instance Ge_xSe_y/SiO_2 multilayer structure (Figure 11) [45].
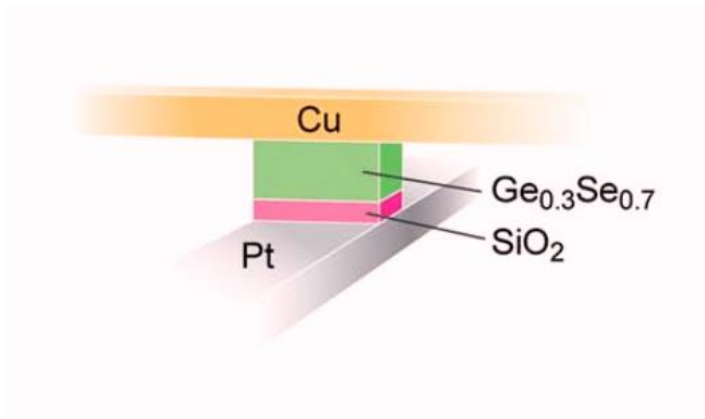
Figure 11: The structure of multilayer Ge$_x$Se$_y$ memory cell [45].

Another method is to preform an electroforming process before the first SET operation. It should be stressed the difference of electroforming in selenide thin layer and oxide thin layer. In oxide thin layer, the filament is firstly created under relative forward high bias, which is referred as electroforming. Nevertheless, the electroforming in selenide thin layer means Ag$^+$ ions are driven out off the thin layer under reversed voltage (Figure 12) [46].
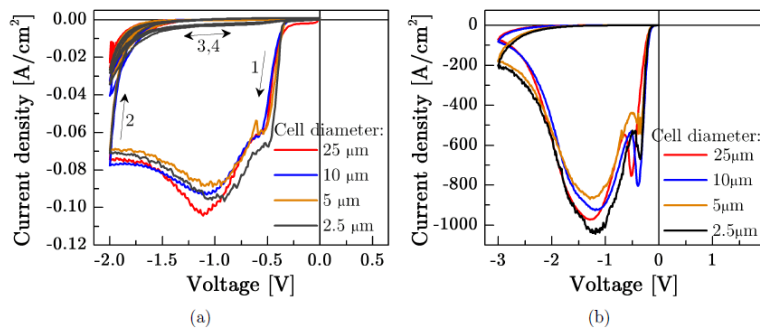
Figure 12: Current density-voltage characteristics of the electroforming process in (a) Ag/Ag-Ge-Se/Pt and (b) Cu/Cu-Ge-Se/Pt cells with varying cell diameter [46].

Except for Ge-S and Ge-Se, Ag or Cu doped Ge-Te binaries are also a common materials for resistive switching. The preparation of Ag doped Ge-Te thin layer can be carried out by the co-sputtering of different components (Figure 13) [47].
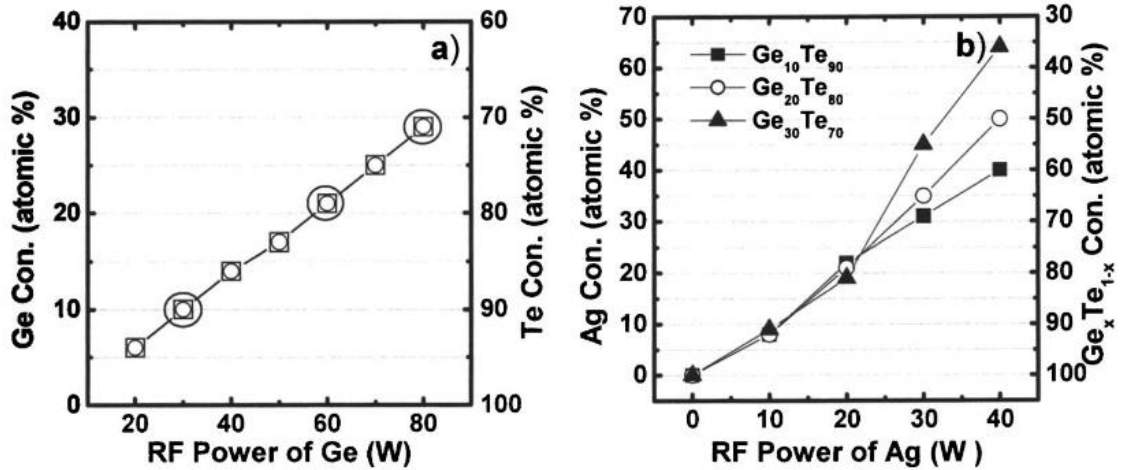
Figure 13: (a) Variation of Ge concentration in Ge_xTe_{100-x} alloys as a function of Ge RF power, (b) Ag concentration in $Ag_x(Ge_yTe_{1-y})_{100-x}$ alloys as a function of Ag RF power [47].

Ge-Sb-Te (GST) thin layers were recently studied as a material for phase change memory [48]. However, the combination of GST and conventional ionic switching layer (CuO_x) can result in an improvement of device behavior. The main reason is the creation of local conductive filament in GST thin layer. Thus, it decreases the randomness of metal filament in CuO_x thin layer (Figure 14) [48].
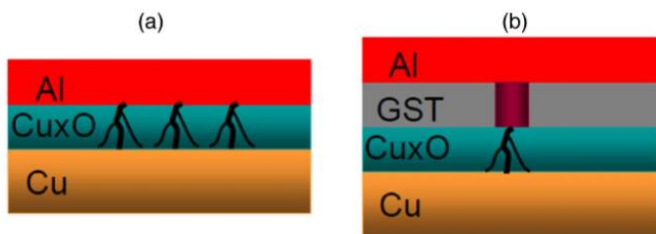
Figure 14: Schematic views for the combined phase change material and resistive switching filamentary conduction model ((a) without and (b) with GST layer) [48].

2.8 The geometry of memory cell

2.8.1 Crossbar structure

The persistent increase of memory integration density expressed by Moore's law illustrates the demand for ever smaller structures. Therefore, crossbar arrays are widely investigated [49]. Non-volatile and resistive switching materials with two stable states such as TiO_2 have been integrated as two terminal memory devices to efficiently create a resistive switching bit pattern [50].

The vertical cross-point architecture presented in Figure 15 can extremely enhance memory density by extending the space for memory cells in the same chip area. Compared to the simply stacked horizontal cross-point architecture, it could be more effective by processing multilayer cell stacks at one time [51].
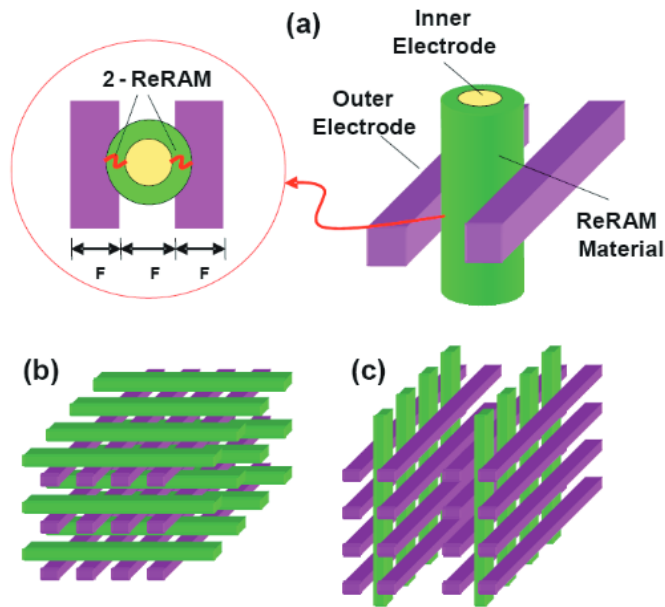
Figure 15: Schematic diagram of (a) an unit vertically-defined ReRAM cell, (b) horizontal cross-point architecture, and (c) vertical cross-point architecture [51].

However, undesirable sneak current can arise from nearby array, causing the 'cross talk' effect [52]. This problem is solved by connecting a diode in series as a selection circuit in unipolar resistive switching [53].

2.8.2 Via-hole structure

The via-hole structure contains an insulating thin layer with holes defined by photoresist lithography. The resistive functional layer is deposited into the holes, which is free of external disturbance. Thus, a better stability of device can be achieved, compared with crossbar structure.

It is necessary to stress it is difficult to completely fill the holes by sputtering or electron beam evaporation, due to smaller size of holes In this case, atomic layer deposition (ALD) can be used to control the deposition of atoms in the atomic level resulting uniform functional and electrode layer (Figure 16).
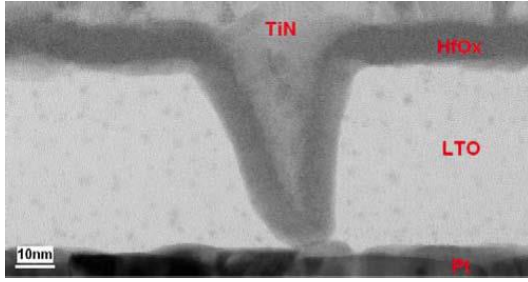
Figure 16: Cross-sectional TEM image of the TiN/HfO$_x$/Pt device [54].

2.9   The parameter for memory device

2.9.1   Write operation

Write DC voltages V$_{wr}$ should be in the range of a few hundred millivolts. The related parameter differs from the material and structure of switching cells, as listed in Table 2. It can be clearly seen that the binary chalcogenide thin layer has lower threshold voltage.

Table 2: The SET and RESET voltage of switching device [55].

System	SET and RESET voltage (V)	System	SET and RESET voltage (V)
Cu/Ge$_{0.3}$Se$_{0.7}$/SiO$_2$/Pt	0.2	Ag/Ge$_2$Sb$_{2+x}$Te$_5$/Mo	1.5
Ag/TiO$_2$/Pt	<0.4	Al/CuO$_x$/Cu	1.5
Ag/SrTiO$_2$/Pt	0.56	TiW/InSbTe/ TiAlN	2.4
Au/ZrO$_2$/Ag	1	Cu/Ta$_2$O$_5$/Ru	3.5
Cu/TaO$_x$/Pt	1	Ti/Cu/ZrO$_2$/Si	4
W/Cu/WO$_3$/Cu	1		
Cu/Mn:ZnO/Pt	0.4		

2.9.2   Read operation

Read DC voltages V$_{rd}$ need to be significantly smaller than write voltages V$_{wr}$, in order to prevent a variation of the ON state resistance during the read operation. Because of constraints by design requirement, V$_{rd}$ should not be less than approximately one tenth of V$_{wr}$.

In the crossbar geometry, two voltage levels are used, which is $1/2$ V_{wr} and $1/3$ V_{wr}. The read time t_{rd} must be in the order of write time t_{wr} or preferably shorter.

2.9.3   Resistance ratio

The resistance ratio is the ratio of resistance between ON and OFF states (R_{ON} and R_{OFF}). Mostly, the resistive switching memory has from 10 to 10^{11} resistance ratio.

2.9.4   Endurance

Endurance is the number of repeatable cycles during the writing and the erasing. As the next generation of memory device, it should be at least 10^6 cycles.

2.9.5   Retention

Retention is the holding time of resistance, which is a key parameter for evolution of memory cell. For the safety of data, the endurance of memory chip must be higher than 10 years. In addition, the memory chip should also be functional at temperatures higher than 85 °C [26].

2.10   The observation of conductive filament

For many devices, the resistive switching effect is described by the formation of conductive filament. Observation of conductive filaments gives a direct advantage for device optimization. The TEM study provides fruitful images, proving the existence of conductive filaments. The study methodology can be divided into two categories: *ex-situ* and *in-situ*.

2.10.1 The *ex-situ* observation

The direct observation of conductive filament is difficult, due to the small diameter and random orientation of filament. Some researchers adopted conductive AFM to study the conductive region from the top side of memory cell. However, the composition and valence of conductive filament cannot be analyzed by this method. Therefore, TEM was utilized, for instance in the Ag/ZnO:Mn/Pt device, as shown in Figure 17. The combination of TEM with EDX spectroscopy revealed that the conductive filament mainly consists of Ag [56].
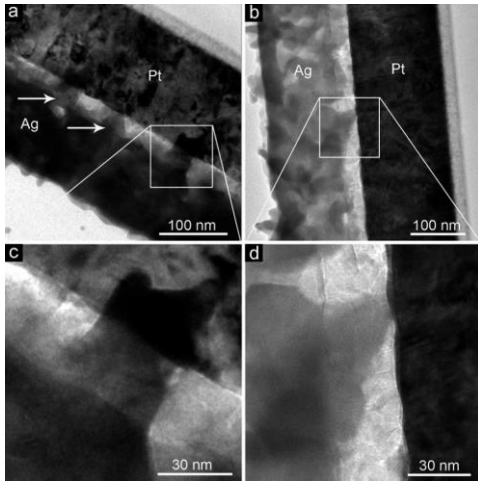
Figure 17: Conventional TEM observation for conductive filaments in the Ag/ZnO:Mn/Pt memory cell that has been switched on [56].

2.10.2 The *in-situ* observation

The existence of conductive filament has been proved by *ex-situ* TEM, while the dynamic of filament growth is only studied by *in-situ* TEM. Yang [56], from Michigan University, reported a study of resistive switching in Ag/a-Si/W device. The images were taken by *in-situ* TEM, during the duration of applied bias. As described in Figure 18, there can be seen the growth of the filament.
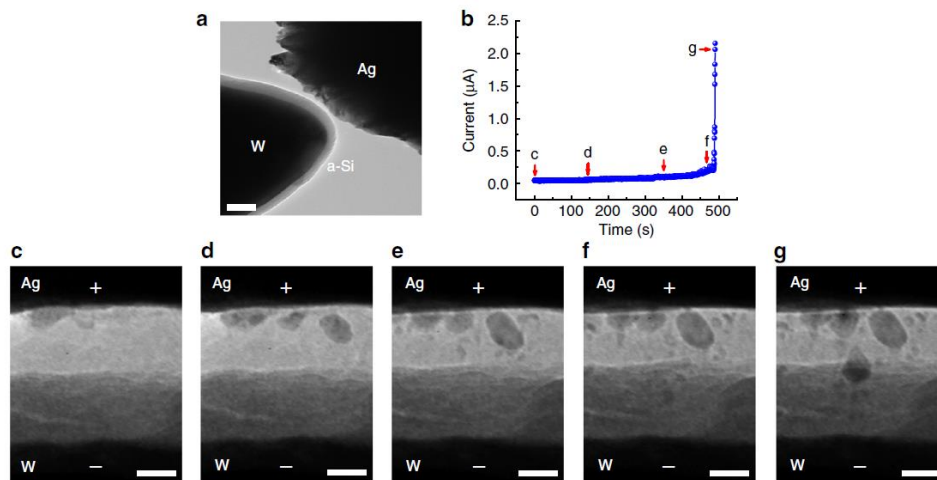
Figure 18: In-situ TEM observation of conducting filament growth in vertical Ag/a-Si/W memories. (a) Experimental setup. (b) I–t characteristics recorded during the forming process at a bias of 12 V. (c–g) TEM images of the device [56].

Chen *et al*. [32] reported a study of conductive filament in ZnO thin layers, in which the dynamic images were recorded by *in-situ* TEM. It can be seen that the filament grows from the anode to the cathode and the filament is proved as ZnO_{1-x} (Figure 19) [32].
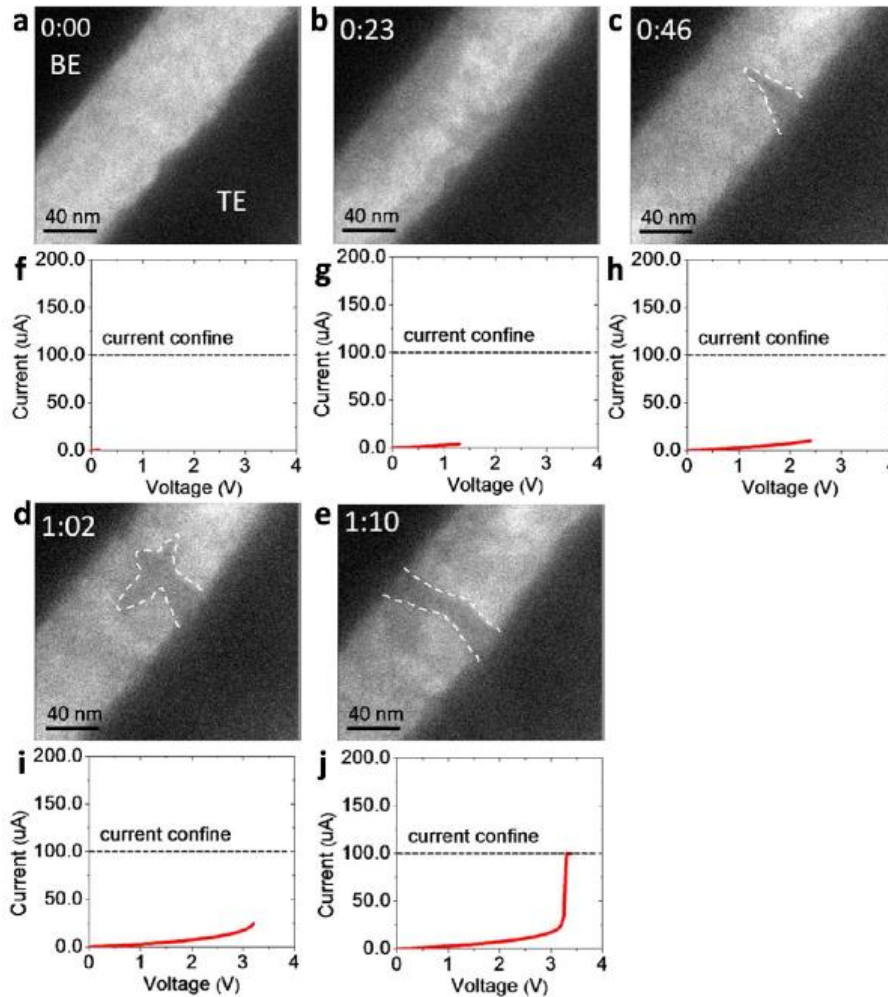
Figure 19: The evolution of conductive filament in ZnO thin layer and its corresponding I-V curve [32].

2.10.3 Observation of filament in chalcogenide thin layer

As the Ag particles are possibly formed on the top of thin layer during ion milling; the preparation of sample for TEM observation is difficult. Arizona State University published a result with images of surface filament by using Ag-Ge-Se thin layer. Two electrodes (Ag electrode and a W tip electrode) were placed with a distance of 370 μm on the surface of sample surface and image was obtained by optical microscope. Dendrite was observed between the electrodes and the current variation was also recorded with large fluctuation. It is explained by the instability of Ag filament and consumption of Ag electrode (Figure 20).
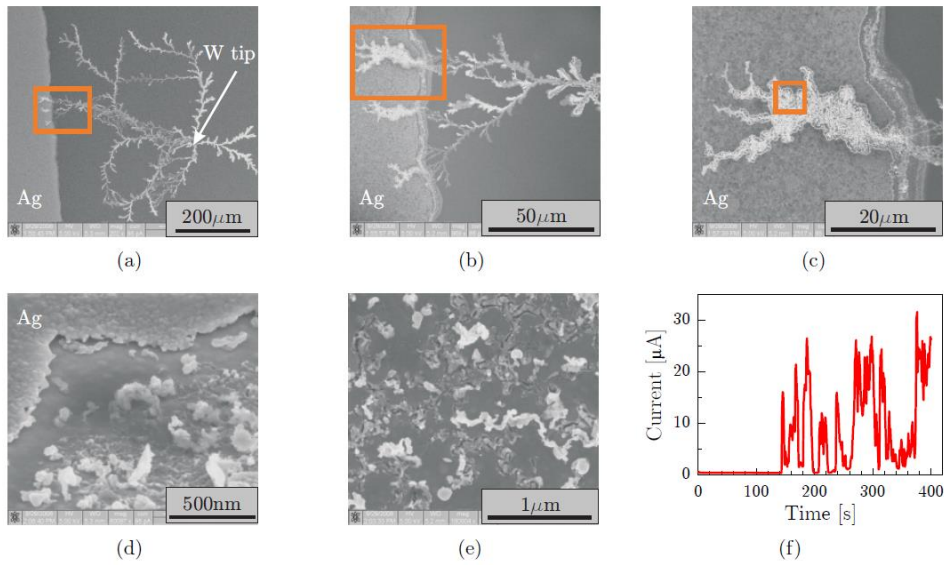
Figure 20: Dendrite growth between a W probe spot and Ag electrodes on the surface of Ag-Ge-S with −4 V applied to the W electrode. (a)-(c) show the morphology of dendrite and interface of dendrite and Ag electrode. (d)-(e) show Ag electrode consumption. (f) Current-time curve during dendrite growth [46].

The morphology of conductive filament and the direction of growth in fast ion conductor have been studied in Cu/Cu-GeTe/Pt-Ir system with *in-situ* TEM imaging. In chalcogenide thin layers (for instance, Ge-Se, Ge-S, Ge-Te, etc.), the dissolution of Ag and Cu can be obtained in high concentrations. Therefore, the Ag or Cu ions can migrate easily under specified bias. As a result, it can be seen that the filaments start to grow form the inert electrode side to the active electrode (Figure 21).
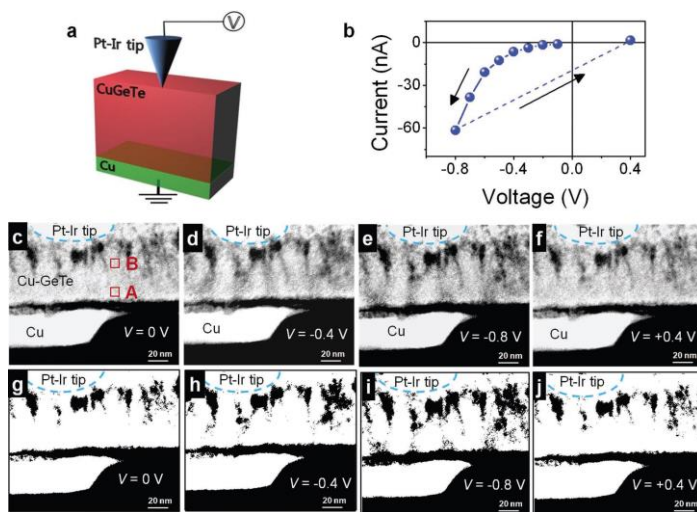
Figure 21: The *in-situ* TEM images of the Cu/Cu-GeTe/Pt-Ir system [57].

2.11 Nanoscale resistive device

Lieber *et al*. [58] fabricated Si/a-Si core-shell structure with crossbar geometry as shown in Figure 22. They adapted two steps of deposition processing: 1) synthesis of Si nanowire with different metal catalyst, 2) deposition of amorphous Si shell. The device exhibits bipolar switching and the size can be 20×20 nm^2. The R_{ON} and R_{OFF} difference is larger than 10^4, and response time is shorter than 100 ns [58].
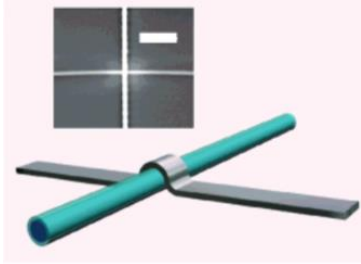
Figure 22: A single memory cell is formed at the cross-point of a Si (blue)/a-Si (cyan) core-shell nanowire (metal nanowire (grey)) [58].

Nagashima *et al*. [59] prepared MgO/Co$_3$O$_4$ nanowire for resistive switching. The device shows stable bipolar switching with 10^8 repeatable cycles.
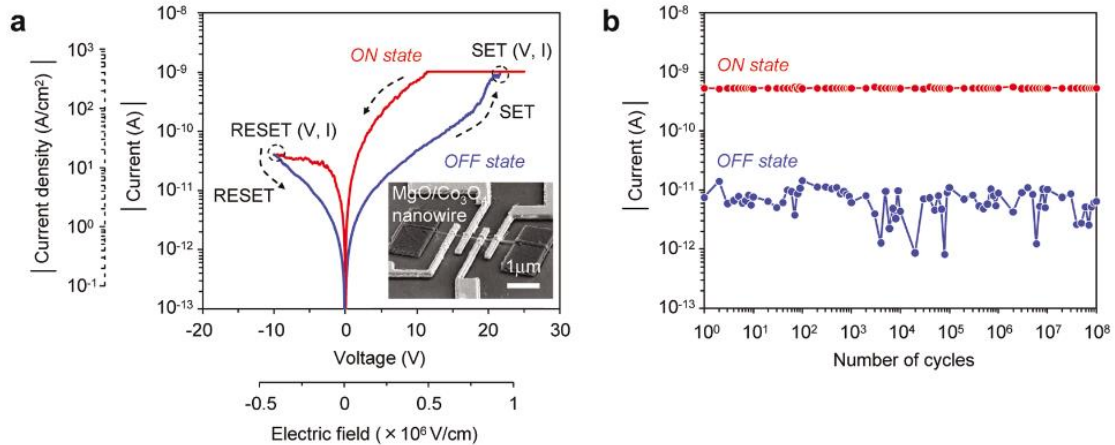
Figure 23: (a) I-V characteristics of MgO/Co$_3$O$_4$ nanowire of the device presented in the inset, (b) the endurance data of MgO/Co$_3$O$_4$ nanowire [59].

Yong *et al*. [60] adopted simple thermal evaporation method to prepare W$_{18}$O$_{49}$ nanowire, and the device structure is Au/W$_{18}$O$_{49}$/W, which shows bipolar response (Figure 24).
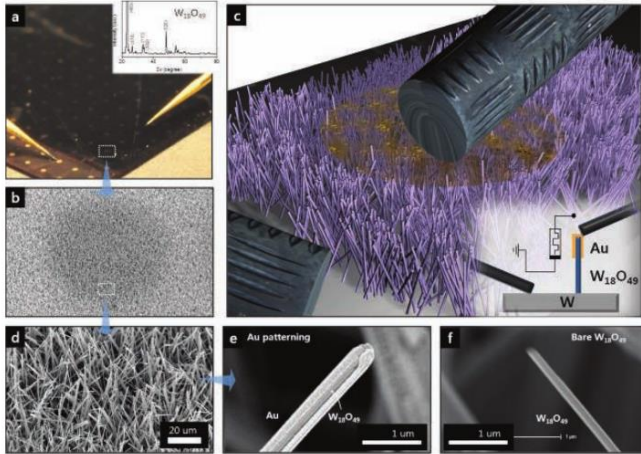
Figure 24: (a)-(f) Structural images of the fabricated W/WO$_x$/Au resistive switching devices [60].

Anodic Aluminium Oxide (AAO) template can assist the growth of nanowires. Lyu *et al*. [61] fabricated 15–90 nm nanowires and tested the property of switching curve (Figure 25).
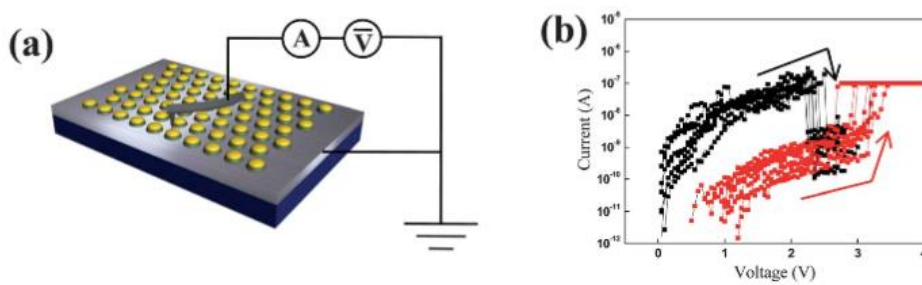
Figure 25:(a) Schematic illustration of devices and measurements setup, (b) I-V curve of resistive switching device [61].

Kolar *et al*. [7] reported an Ag nanowire array by solution-based electrochemical deposition into AAO membrane. The Ag nanowires served as a source of Ag for photo doping and active electrode as well. The experiment proves that the Ag nanowire array provided higher R$_{ON}$ and R$_{OFF}$ difference, in comparison with the device with flat Ag electrode (Figure 26) [7].
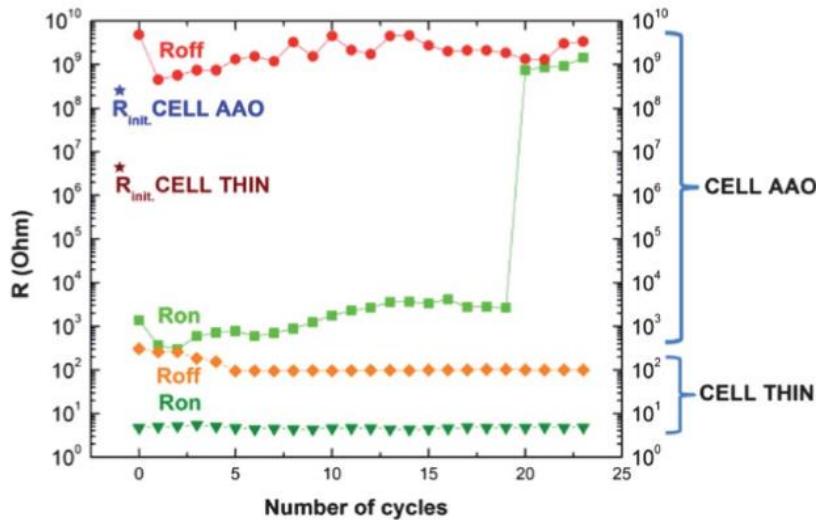
Figure 26: Comparison of resistance data between the AAO device (CELL AAO) and the plane Ag electrode (CELL THIN) [7].

3 Experimental part

3.1 Preparation of thin layers

Table 3 shows the materials selection for different geometries of electrodes and electrolytes. The top electrodes can be divided into two categories: fixed and floated type, in which fixed top electrodes are prepared via thermal evaporation and floated electrodes, relied on the equipment probe. The W and Pt layer was prepared by magnetron sputtering and Al_2O_3 layer was prepared by PLD.

Table 3: The electrodes and electrolytes of different geometries.

Geometry	Top electrode	Electrolyte	Bottom electrode	Electrode Size
Spot	Al (100 nm)	Ag doped AsS_2 (237 nm)	Ag (300 nm)	Diameter 1 mm
Crossbar	Ag (100 nm)	Ag doped $GeSe_2$ (120 nm)/Al_2O_3 (2–3 nm)	W (150 nm)	Width 0.1 mm
Needle contact	W coated needle	Ag doped AsS_2 (230 nm)	Ag (100nm)	Needle radius 100 μm

Atomic force microscope contact	Tip of atomic force microscope	Ag doped AsS_2 (230 nm)	Ag (100 nm)	Tip radius 20–30 nm
Via-hole geometry	Ag (100 nm)	Ag doped $GeSe_2$ (120 nm)	Pt (50 nm)	Diameter 5 μm

The parameters of thermal evaporation are presented in Table 4. Instrument UP 311-B was used for depositions. Thickness of the layers was monitored *in-situ* by quartz crystal microbalance. The chalcogenide thin layer was deposited from glassy ingot, which was prepared in advance. W layer was prepared via magnetron sputtering under the initial vacuum of 10^{-4} Pa and power 65 W for 20 minutes, which resulted in thickness of 150 nm. During the sputtering process, large amount of heat was generated. In order to prevent the damage of sample, the W thin layer can only be used as bottom electrode. The Al_2O_3 layer was prepared by pulsed laser deposition at residual pressure of 3.9×10^{-4} Pa and pulse energy of 215 mJ. The Al_2O_3 layers deposition was preformed in two runs, in which the first run was done with 40 second deposition on silica wafer for ellipsometry measurement, in order to calibrate the layer thickness. Based on the results from the ellipsometer, the ultra thin layer (approx. 2nm) was made with 7 second deposition on the W surface.

Table 4: The deposition parameters of thermal evaporation.

Material	Pressure before deposition (Pa)	Evaporation rate (nm/s)
Al	10^{-4}	1–2
Ag	10^{-4}	1–2
AsS_2	10^{-4}	<1
$GeSe_2$	10^{-4}	<1

3.2 Photo doping and dissolution

The Ag^+ ions are commonly introduced into chalcogenide thin layer through photo diffusion and dissolution, and the basic mechanism has been introduced above and shown in Figure 27. In the case of Ag/GeSe$_2$ bilayer, an ultrathin layer (10 nm) is deposited onto the surface of GeSe$_2$ thin layer. As the ultrathin Ag layer is semi-transparent, the sample can be illuminated from the top side, and Ag ions diffuse into GeSe$_2$ thin layer from top to bottom side until the Ag layer is completely dissolved. For AsS$_2$/Ag bilayer, the AsS$_2$ thin layer is deposited onto the surface of the Ag thin layer. The Ag ions are diffused from the bottom to the top side. As the reflection of Ag layer, it can be found that the photo diffusion is much easier with AsS$_2$/Ag bilayer, rather than Ag/GeSe$_2$ bilayer. Therefore, UV illumination (400 nm) was utilized with Ag/GeSe$_2$ bilayer, in order to improve the efficiency of photo diffusion. Fluorescent illumination of the projector is used for AsS$_2$/Ag bilayer with the CuSO$_4$ solution to remove the infrared radiation. However, the dose of illumination is necessary to be controlled, avoiding the creation of Ag particles at the surface of thin layer, shown in Figure 9.
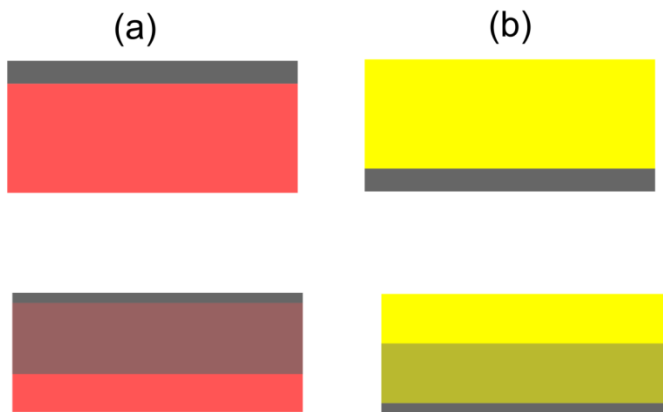
Figure 27: (a) GeSe$_2$ and (b) AsS$_2$ thin layer before and during photo diffusion and dissolution.

4   Characterization methods

4.1   Electric pulse measurement

The switching behaviour was tested by Keithley 2602 SourceMeter, which offers precision DC, pulse, and low frequency AC source-measure testing [62].

The generated pulse was programed by the software Test Script. The schematic sequence of pulses is shown in Figure 28. Several important parameters can be found, such as: the

maximum voltage U_{max}, the minimum voltage U_{min}, the voltage step ΔU, the pulse length t_{pulse}, the delay after each pulse Δt and the delay after each cycle $\Delta t_{After\ cycle}$.

Figure 28: The parameter of pulse measurement.

4.2 SEM

The SEM images were taken by JEOL JSM7500F. JEOL JSM7500F provides topographical magnifications from ×25 to ×1,000,000. The specimen was fixed onto the sample holder, either by silver paste or conductive tape. During SEM analysis, the non-conducting chalcogenide sample is irradiated with an electron beam, resulting in accumulation of static electric charges. This static charge influences the electron signals and hence deteriorates the image information. However, such phenomenon is not obvious in Ag doped chalcogenide thin layer [63].

4.3 AFM

The AFM images were taken by conductive atomic force microscope (AFM Solver Pro M, NT-MDT; Russia) with a silicon probe coated with the Cr/Pt layer. It can be applied to measure the morphology of different varieties of material, for example thin layers, polymers, semiconductors, and biological samples [64].

The probe was defined as the negative electrode and Ag layer as positive electrode in conductive AFM mode. The current flow in this work was considered from the positive electrode to the negative electrode. The tapping mode was selected to investigate the *in-situ* surface morphology of the memory cell, changes or the spread currents.

4.4 Optical microscope

The colourful low magnitude images were taken by optical microscope Olympus BX51 and with the magnification from ×10 to ×100.

5 Main results and their discussion

5.1 The resistive switching with spot geometry

5.1.1 Introduction

The spot geometry was the simplest memory cell, in which the outline of electrode is defined via photoresist lithography or stencil mask. The advantage of spot electrode is easy and cheap to fabricate and it can be applied to almost all kinds of materials. For oxide thin layer, the graphite electrode can be prepared via photoresist lithography, as it is compatible with solution, for instance silicon dioxide thin layer. However, Ag doped chalcogenide thin layer is prone to be delaminated from its substrate when it is in contact with organic solutions. In our case, stainless stencil steel mask was utilized during evaporation of AsS_2 thin layer (Figure 29). The material of top electrode is considered as another important factor, due to the fragile chalcogenide thin layer. Impropriate material or preparation method can lead to the thin layer to be peeled off or broken. Therefore, evaporated Al is recommended as the top electrode for its compatibility with chalcogenide thin layer. Nevertheless, Al is reactive with oxygen gas from atmosphere. Due to this fact it is necessary to store it in vacuum.
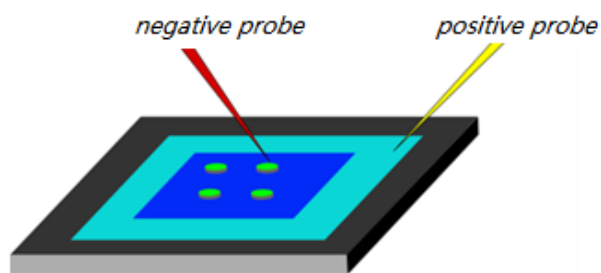
Figure 29: The experimental setup. (The light blue colour represents the Ag electrode, the dark blue represents Ag-doped AsS_2 chalcogenide layer, and the green spots represent the Al electrodes).

5.1.2 Experimental results

The diameter of upper Al electrode was 1 mm, in accordance with its area 0.785 mm^2. It can be seen from Figure 30 (a) that the R_{ON} and R_{OFF} difference is approx. $\approx$10. Meanwhile, good repeatability can be found as up to 5,000 cycles.

The nature of resistance and repeatability difference reflects the key role of current density. High current density may cause excessive Joule heating, which accelerate the aging of memory cell. Figure 30 describes the switching cycles in Ag/Ag doped AsS$_2$/Al (spots) device. In AB stage, the current level is in 10^{-3} A, during which the conductive filament is not completely formed. Atomic conductance can be found in BC stage showing discrete resistance. The filament is formed completely at point C, which shows the resistance in 10^{-2} Ω. In stage CD, the linear dependence shows the metallic conductivity. After point D, the filaments start to be dissolved. During stage DE and EA, it is noticeable that the filament cannot be completely dissolved. Generally, the triangle ABC is smaller than the triangle DEA, in which the V_{SET} (0.22 V) is lower than the absolute value of V_{RESET} (0.25 V). It may be explained as the easier formation of filament than dissolution of filament. Also large electrode might induce the leakage of current, in electric deposition of Ag particles. In summary, although the spot geometry is simple, it offers much stable switching repeatability.
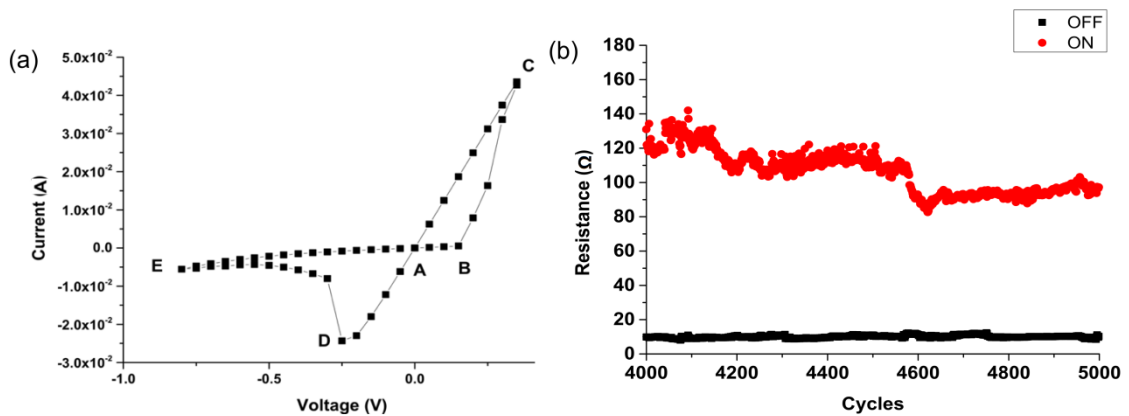
Figure 30: (a) The I-V curve of resistive switching, (b) the dependence of R_{ON} and R_{OFF}.

5.1.3 Summary

The switching cell with spot geometry can be simply fabricated and the switching behaviour is very stable. However, due to the relative large electrode, the R_{ON} and R_{OFF} difference is low. Therefore, spot geometry is not suitable for application.

5.2 Crossbar geometry

5.2.1 Experimental results

The crossbar geometry is fabricated with two line-shape electrodes (Figure 31) in crossing and the electrolyte with buffer layer is inserted between electrodes. The electrodes are referred as bit and word line, and cells can be selected with different bit and word line. The purpose of buffer layer is still in debate [45] , [23]. In our study, we used an ultrathin layer of Al_2O_3 (2–3 nm), as buffer layer. Two sets of samples were fabricated with different positons of Al_2O_3 layer, and different I-V curves and impedance were presented, in order to investigate the function of buffer layer.
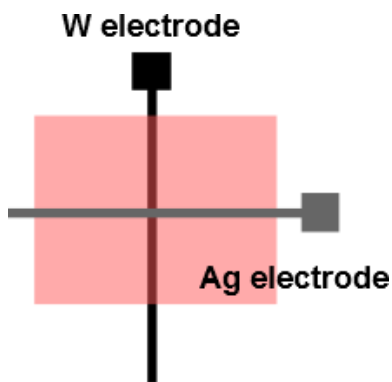
Figure 31: The planar view of crossbar geometry.

The cross section view of INERT BUFFER and ACTIVE BUFFER are presented in Figure 32 (a) and 32 (b). The conductive filament is expected to be formed in the chalcogenide GeSe layer rather than Al_2O_3 layer. Figure 32 (c) shows the atomic microscope image of Al_2O_3 layer deposited on the W electrode. The Al_2O_3 layer is expected to consist of particles or islands, due to the short duration of laser deposition. It can be found from the AFM image of Al_2O_3 layer, that the surface is formed by particles ranging from 0 to 12 nm in height. It is much larger than the expected value of ultrathin Al_2O_3 layer from calibration of ellipsometry (2 nm) (Figure 32 (d)). Therefore, such roughness might be contribution of both Al_2O_3 layer and W layer.
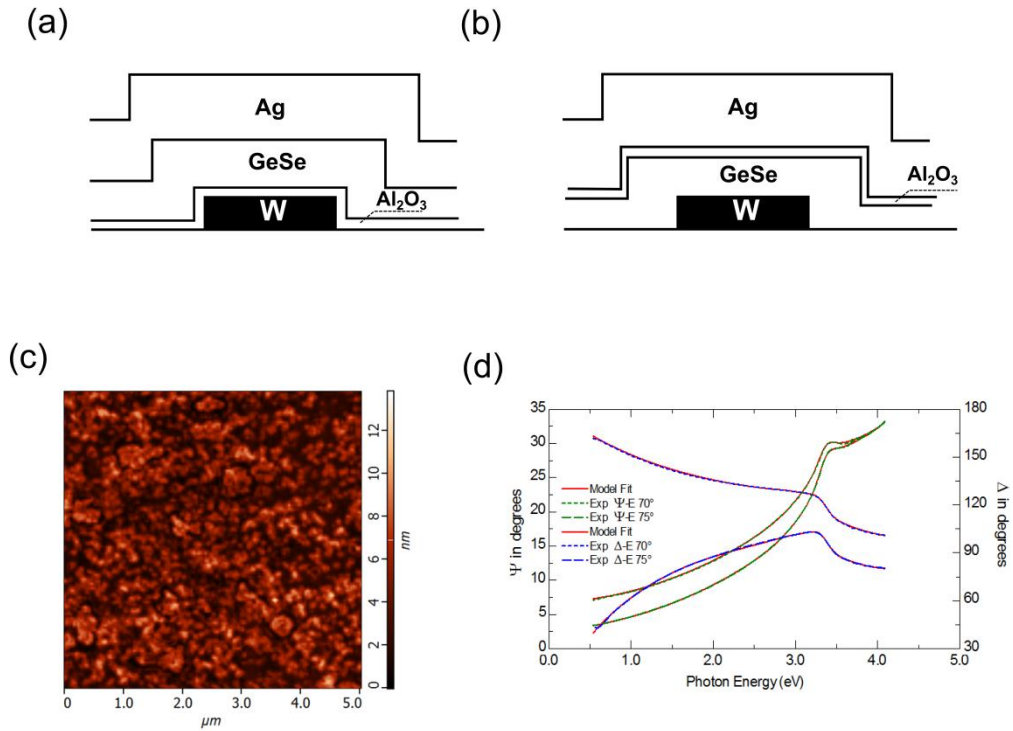
Figure 32: (a) The cross section view of INERT BUFFER device, (b) the cross-sectional view of ACTIVE BUFFER device, (c) the atomic force microscope image of ultrathin Al_2O_3 layer (2 nm) deposited onto W layer, (d) ellipsometric data fit for Al_2O_3 layer used for calibration (14 nm, with duration 40 s).

The impedance spectroscopy of the sample was measured with $W/Al_2O_3/GeSe/W$ stacking, which the resulting spectrum is shown in Figure 33. The resistance is 7.4×10^9 Ω. Only one semicircle can be identified, which indicates the Al_2O_3 layer does not completely cover the W electrode [65].
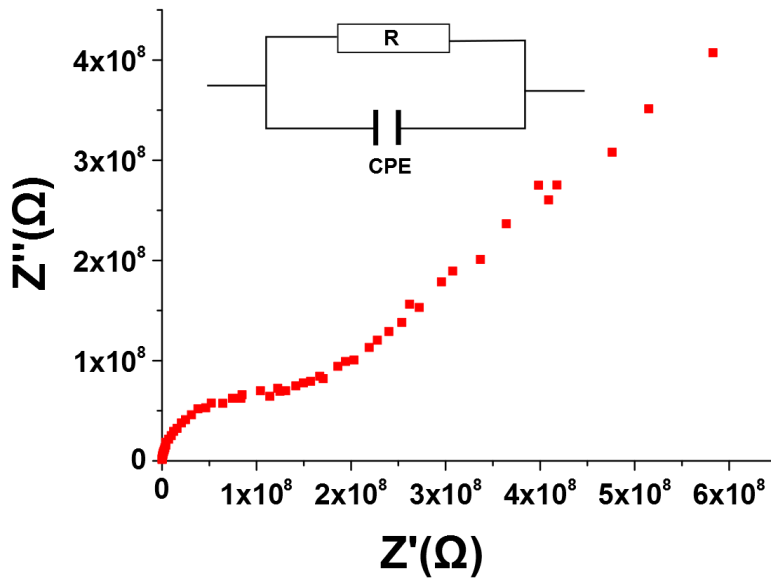
Figure 33: The impedance spectrum measurement of sample and equivalent circuit is presented in Figure inset.

Figure 34 shows the I-V curve of resistive switching, in which the bias range and current limit are set differently between two samples. INERT BUFFER sample (see Figure 32) shows typical resistive switching cycle with SET bias approx. 1.2 V and RESET bias approx. −0.4 V, which is comparably higher than that described in literature [66]. Such difference is possibly caused by the buffer layer in reducing the leakage current and therefore, improving the SET bias. The linear independence of I-V curve proves the existence of metallic conductivity filament in INERT BUFFER sample. On contrary, the I-V curve in ACTIVE BUFFER sample (see Figure 32) exhibits diode behaviour and fluctuates from 1.0 V to 3.0 V and the corresponding threshold bias for current ramping up is 1.2 V. Moreover, the current limit is not set for ACTIVE BUFFER sample and current shows the increasing tendency up to the maximum bias of 3.0 V. Therefore, it can be assumed that no metallic filament is formed in ACTIVE BUFFER sample.
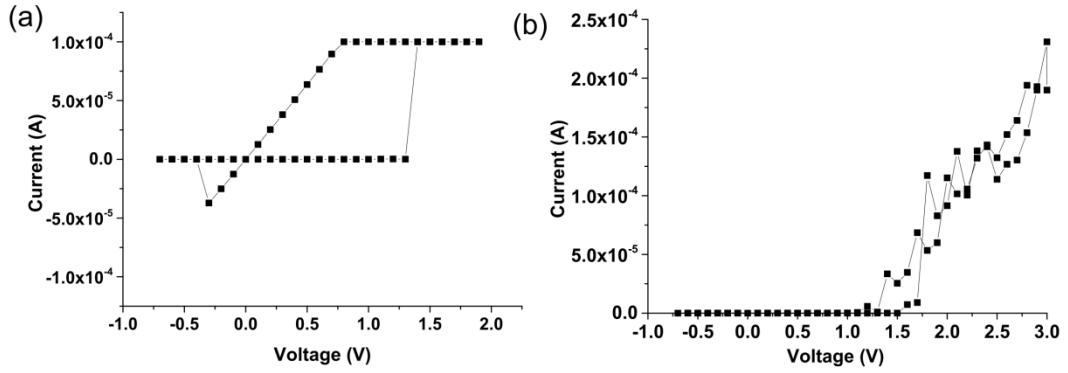
Figure 34: I-V curves: (a) INERT BUFFER (b) ACTIVE BUFFER sample.

R. Soni [45] reported buffer layer as an intermedia for filament growth and C. Schindler [23] reported that it limits the diffusion of Ag ion. In our case, we put forward a different opinion that the function of the buffer layer is to separate the contact area of electrode into several small independent regions. Thus, ultrathin island-like Al_2O_3 layer is designed as buffer material for its selective possibility to form Ag filament and Ag concentration is kept almost constant between the INERT BUFFER sample and ACTIVE BUFFER sample through photo doping process, in order to prove its influence.

As described above, the positon of buffer layer determines the behaviour of device (resistive switching or diode), and the mechanism is explained in Figure 35. As the buffer layer may not complete cover the underlying thin layer, it would be more reasonable to assume that the filament is not able to be formed within buffer layer as is schematically shown in Figure 35(a). As the result of that, the Ag ions tend to nucleate in the uncovered regions, under bias, which finally results in formation of the conductive filaments. Figure 35 (b) shows the situation of buffer layer lies at interface of Ag electrode and Ag doped GeSe layer. Under bias, the Ag ions are less likely to be nucleated either at the Ag or W electrode. Instead, Ag ions might be accumulated at the Ag electrode and causing polarized distribution.
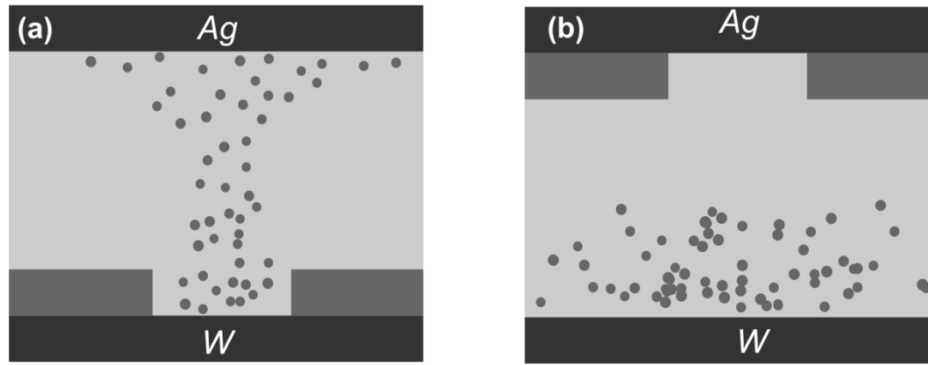
Figure 35: The schematic picture of mechanism in (a) the INERT BUFFER sample and (b) ACTIVE BUFFER sample.

Furthermore, the redox reaction of Ag species does not proceed; instead, the cell is turned into a capacitor. The increase of the device capacitance would lead to large charging current. In summary, the creation of filaments highly depends on the nucleation, which can be facilitated by inducing isolated regions of inert electrode. Moreover, it also proves the growth of filament is started from the inert electrode towards the active electrode, which fits the TEM observation result described in literature [56].

5.2.2 Summary

Two samples (INERT BUFFER, ACTIVE BUFFER) are designed to study the function of buffer layer. Due to the different stacking sequence of buffer layer, the resistive switching behaviours of devices are completely different, which the current increase in INERT BUFFER and ACTIVE BUFFER might be caused by metal filament and capacitance change, respectively. The main function of buffer layer is to facilitate the nucleation of filament.

5.3 Needle contact geometry

5.3.1 Introduction

The device fabrication with needle contact geometry is similar as the spot geometry: The 300 nm Ag thin layer over coated by 237 nm AsS_2 thin layer was carried out onto silica glass substrate without mask. Insulating AsS_2 thin layer was then modified into ion conducting Ag_xAsS_2 by photo-induced dissolution and diffusion of Ag due to exposure by a mercury lamp illumination for 30 minutes under pure N_2 atmosphere (4N purity).

The measurement was carried out by Keithley 2602, in which the positive W needle probe was contacted with the Ag electrode and negative W probe needle was contacted with the sample surface. Therefore, the negative probe needle behaves as a floating electrode, and the

size of needle tip (radius 100 µm) determines that of negative electrode. In contrast to spot geometry, needle contact geometry is simpler (without preparing top electrode), and contact region can be observed under SEM for further analysis. Meanwhile, the disadvantage is the risk of thin layer penetration by needle probe.

5.3.2   The resistive switching curve

Figure 36 shows the schematic picture of experiment setup and the pulses. It can be clearly seen that the maximum voltage and minimum voltage was not set with the same value, in order to facilitate the dissolution of filament. The surface morphology was observed by optical microscope Olympus BX51 and by scanning electron microscope JEOL JSM7500F with secondary electron mode.
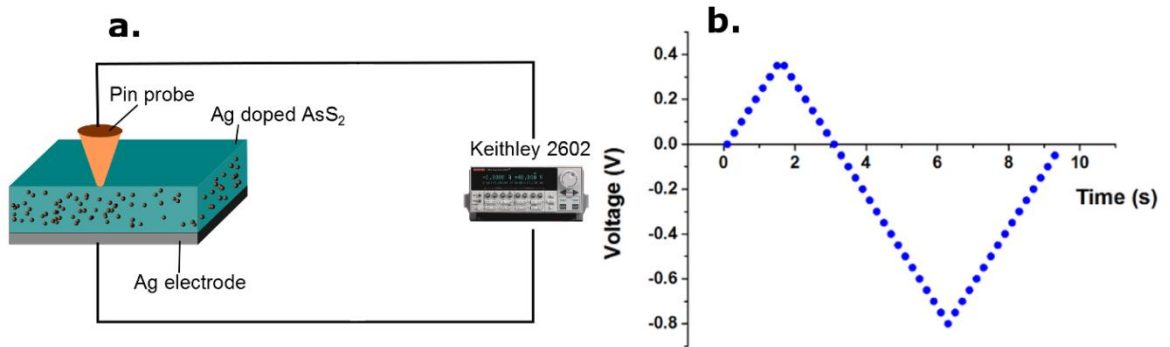
Figure 36: (a) The schematic picture of experiment setup, (b) the pulses of algorithm.

The experimental result contains electric testing (I-V and I-t curve) and observation of surface morphology. The algorithm provides the SET voltage (V_{SET}). The double voltage algorithm provides formation of conductive filament below SET voltage (V_{SET}).

Figure 37 (a) describes the I-V curve in one cycle. The SET voltage is 0.35 V, which can be understood as the conductive filament formation within single pulse length (0.1 s). It can be seen that SET voltage (V_{SET}) is much smaller the RESET voltage (V_{RESET}), and the filament after RESET process is not completely dissolved. The conductivity of filament is not linear, demonstrating the "leakage" of current. The term "leakage" means the current do not only flow via filament but takes part in the other process, for instance redox reaction of Ag ions.
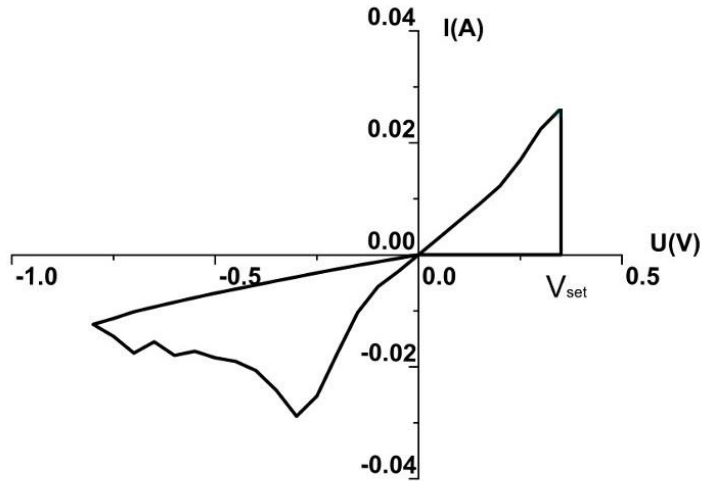
Figure 37: I-V loop curve of Ag/AgAsS$_2$sample.

5.3.3   The observation of sample

5.3.3.1   The front side image of sample

The direct observation of conductive filament in chalcogenide thin layer has been reported by the help of in situ TEM in many papers [32]. The conductive filament was also observed in Ag/H$_2$O/Pt structure under optical microscope [21]. As discussed above, our floating electrode facilities the observation of sample surface before and after creation of the filament. The filament was set as "ON" state, before surface observation. After surface scanning, the sample was broken by diamond tip impact and the cross section was prepared for SEM observation.

Figure 38 shows the surface morphology of the Ag-doped AsS$_2$ thin layer After SET operation. In Figure 38 (a), Ag particles with different size are apparent that were deposited near to the contact point (labelled as "b"). Figure 38 (b) shows SEM image of this corresponding region highlighted in Figure 38 (a), which shows more details about the Ag particle precipitation induced by the tip of pin probe. The imprint of a tip has a diameter of approx. 20 µm. Figure 38 (c) and Figure 38(d) shows the SEM image of silver particles with different sizes corresponding region marked in Figure 38 (a), which might be induced by leakage of current.

The cross-sectional view presented in Figure 38 (e) shows several Ag filaments in the AsS$_2$:Ag thin layer, and Figure 38 (f) shows the enlarged image of the box of Figure 38 (e). On the top of thin layer, a layer consisting of series of Ag particles is shown. As the Ag layer was bonded with the chalcogenide layer, it is impossible to distinguish each component. It has

been reported that the filament itself could increase the mechanical stress to the thin layer [67]. However, no mechanical delamination of the layer was observed in the filament region.
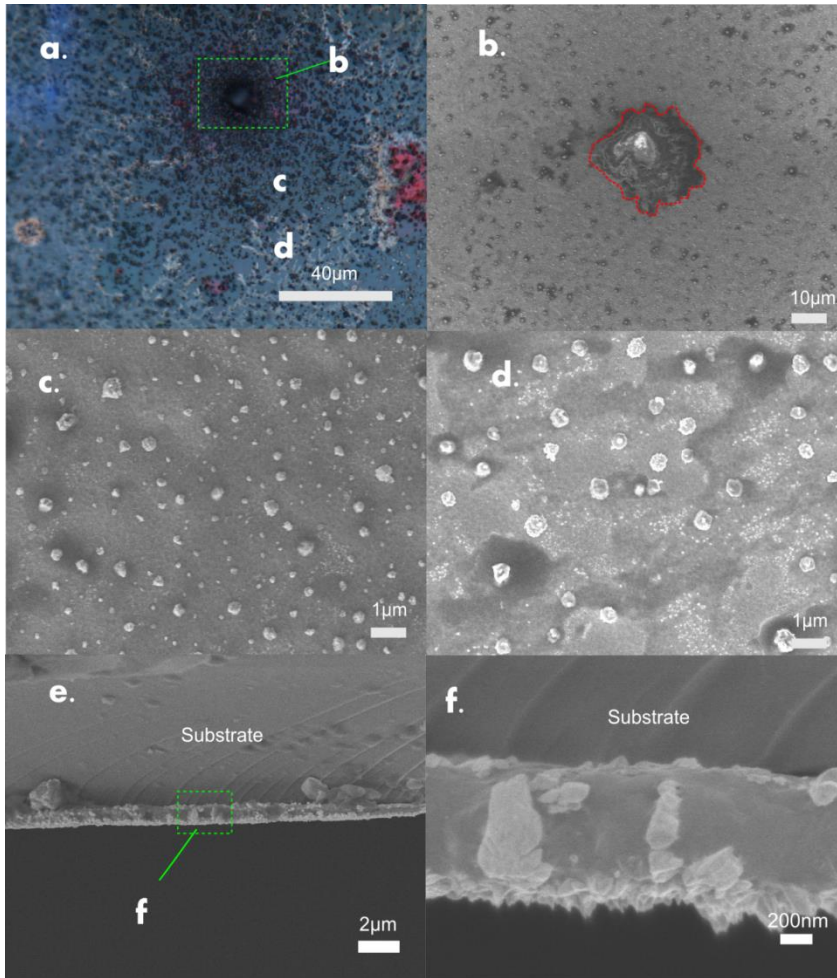
Figure 38: The surface morphology of thin layer memory cell, (a) Optical image of pin probe contact region, (b) SEM image of pin contact point, (c) SEM image of surface particles, (d) SEM image of tree branching, (e)-(f) cross-sectional images by SEM showing Ag filaments in detail.

5.3.3.2 The back side of the sample

As described in reference [20], the decay of memory cell can be due to the contact loss of Ag electrode. Thus, the SEM image of back side electrode is an important evidence. The memory cell was "scotch taped" to another glass substrate and peeled off, in order to observe the back side of Ag electrode. As shown in Figure 39, the Ag electrode was porous, and multiple islands can be identified. The loss of Ag can be explained either by Ag dissolution during photo doping or the oxidation and migration under external voltage. The further development

of Ag "etching" might cause the completely loss of electrode contact, resulting in a constant high resistance at last.
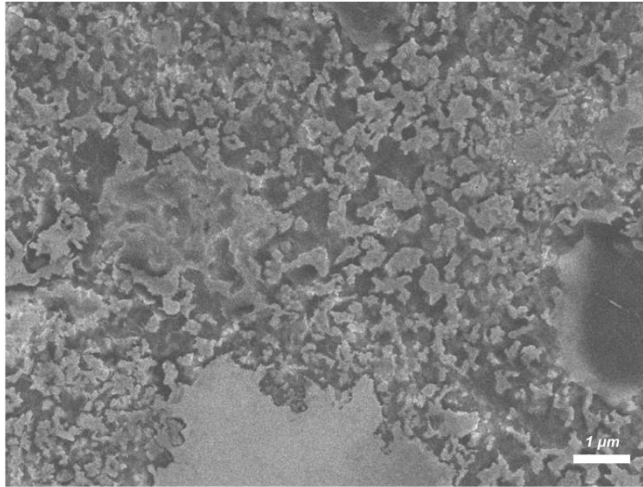
Figure 39: The SEM image of Ag electrode from the back side after switching.

From Figure 40, it can be seen that cross section of multilayer thin layer, in which photo doped AsS_2 layer, Ag layer and silica substrate are stacked from the top to the bottom. Due to the distribution of electric field, the "etching" of Ag thin layer shows different tendency. The Ag reduction marked on the right side is much heavier than the left side and a "hole" in Ag layer can be identified. The contact loss happened between the silica substrate and Ag layer, rather than the Ag layer and chalcogenide thin layer. In the other words, even though the Ag layer converted into Ag ions and migrated into the chalcogenide thin layer, the conductivity was still maintained with Ag layer. However, the memory cell would be fragile, after Ag layer reduction.
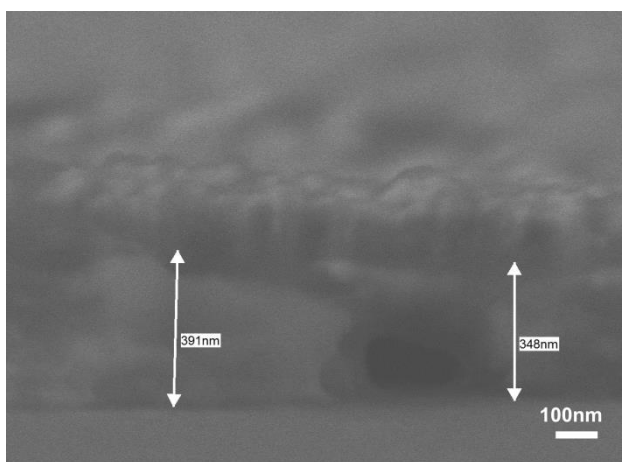
Figure 40: Cross section of multilayer thin layer ($AgAsS_2/Ag$).

5.3.3.3 Electron induced particle creation

It is worth to mention an electron beam induced particle formation was observed, during SEM imaging. Photo surface deposition has been known for chalcogenide thin layer, on which Ag particles are deposited during the light exposure. Photo illumination provides main driving force, in comparison with electrons emitted from SEM [39]. During imaging, we found a similar effect, which an Ag deposition caused by electron beam emitted form SEM gun. A test was designed with different exposure time and accelerating voltage on photo doped AsS_2 to clarify the phenomena. The similar effect was also observed in TEM, in which the accelerated voltage is much higher than that in SEM [68]. However, it is still interesting to know the dynamic for Ag particle growth, as it may affect the SEM observation of Ag doped AsS_2 thin layer.

The SEM image was taken by JEOL JSM7500F and the relevant parameters are shown in Table 5. The JEOL JSM7500F is an ultrahigh resolution field emission scanning electron microscope (FE-SEM). The improved overall stability of the JSM7500F enabled us to readily observe our specimen at magnifications up to ×1,000,000 with the guaranteed resolution of ≈1 nm. It can be seen that the exposure time was 300 s under ×100,000 magnifications (compared with 600 seconds under low magnification).

Table 5: The parameter of experiment with SEM.

Magnification	Time for image (seconds)	Voltage (kV)	Mode
×20,000	0, 30, 60, 90, 120, 180, …, 600	15	Secondary electrons
×100,000	0, 30, 60, 90, 120, 180, …, 300	15	Secondary electrons

Figure 41 shows the generation of Ag clusters, under the exposure of electron beam emitted from electron gun of SEM. In Figure 41 (a), there were some Ag nuclei deposited on the surface, which were developed from photo doping and photo surface deposition. From Figure 41(b) to Figure 41(f), most of Ag clusters were grown from nuclei and the growth dimension was along three dimensions. The situation was similar as heterogeneous nucleation of crystal

[69]. Nevertheless, the morphology of Ag clusters do not share any common geometry and the scale of Ag clusters varied from approx. 1 μm to 100 nm in Figure 41 (f).
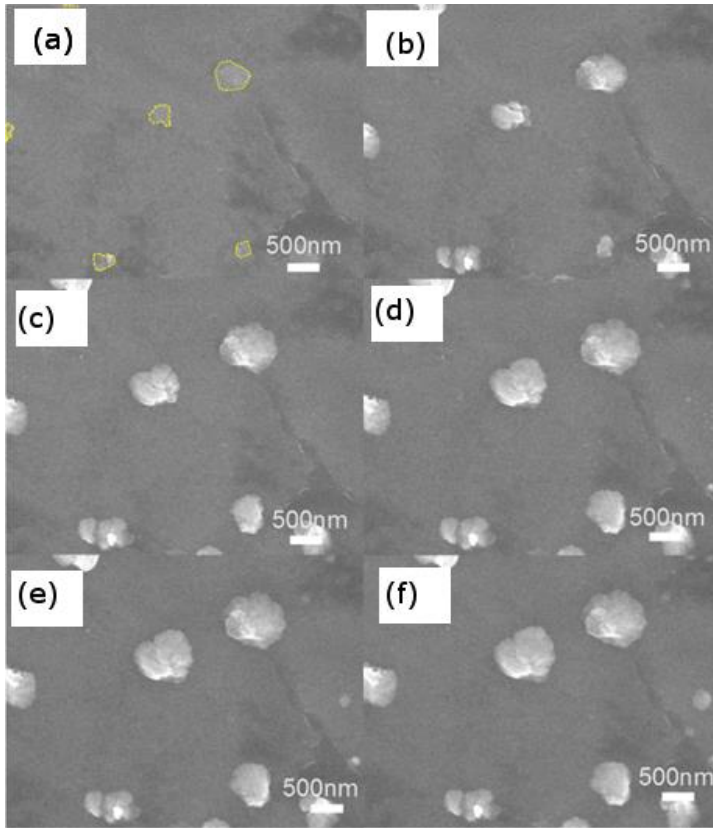
Figure 41: The selected SEM images (×20,000) of Ag clusters; (a) 0 s, (b) 90 s, (c) 180 s, (d) 360 s, (e) 480 s, (f) 600 s; the nuclei are highlighted with yellow circle.

Figure 42 shows the static data regarding with total number and the maximum diameter of Ag clusters obtained from SEM image (Figure 41). It can be seen that the number of Ag clusters was quite stable in the time from 0 to 600 s, which increased only from 6 to 8. During this time, the maximum diameter of Ag clusters increased from approx. 450 to 800 nm in the initial 200 s, then kept stable at 900 nm till 600 s. Therefore, during 200 s, the growth of Ag clusters was the rate dominating process, and the equilibrium size of Ag clusters was obtained from 200 s to 600 s. As discussed above, the total kinetic of the process resembles heterogeneous nucleation [69]. Clearly, most of Ag clusters grew up from photo-induced nuclei. However, infinite dimension growth did not continue under prolonged exposure of electron beam.

Figure 42: The statistical data obtained from SEM image with ×20,000 magnification. (a) The number of clusters developed with time per area of approx. 1.2×1.2 μm^2 (b) The maximum diameter of clusters developed with time per area of approx. 1.2×1.2 μm^2.

Apart from the 'heterogeneous nucleation', a weak homogenous nucleation process can also be observed from Figure 43 (a) to (f), in which the embryos formed under electron beam from SEM. Figure 43 shows the enlarged image of Figure 41 creation from 0 seconds till 360 s under ×100,000 magnification. From Figure 43 (a) to Figure 43 (b), the Ag ion started to agglomerate and several small nuclei, shown in yellow circles, had formed. Nevertheless, it can be found the initial nuclei did not overcome a critical size, i.e. they were not developed into clusters. In next step they were replaced by a new large single nucleus which overcame critical dimension of crystal formation in Figure 43 (c). And in Figure 43 (d), the larger nucleus had developed into an Ag cluster. Only the nuclei comprising the enough size of dimension can grow into Ag cluster.
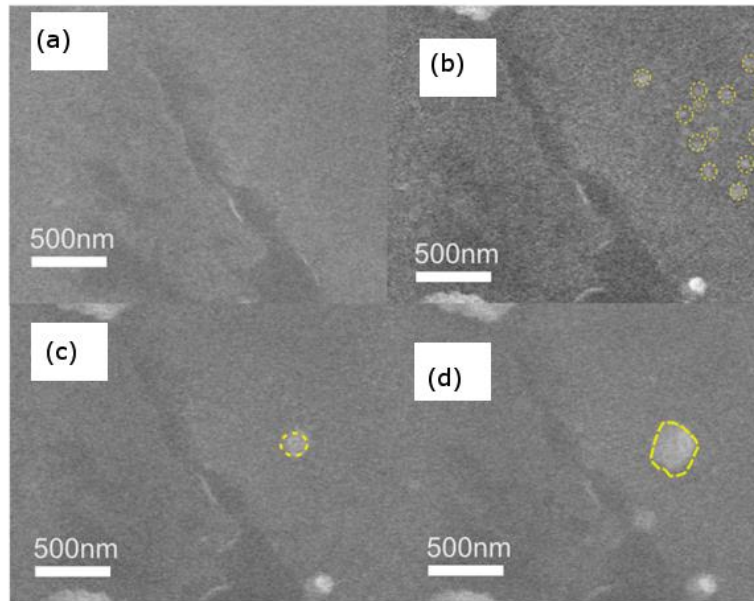
Figure 43: The enlarged SEM image (×20,000) of Ag cluster formation; (a) 0 s, (b) 360 s, (c) 480 s, and (d) 600 s.

Figure 44 shows the image of Ag cluster growth under high magnification (×100,000). The region for observation was selected without nuclei, as shown in Figure 44 (a). All the Ag clusters were induced by the electron beam form SEM. It is noticeable the Ag cluster in red circle, which appeared in 150 s in Figure 44 (b). At 180 s, Ag cluster in yellow circle appeared and the dimension of Ag cluster in red remained unchanged. However, in Figure 44 (d), the Ag cluster in yellow circle grew up, while the Ag cluster in red circle was partially dissolved back into thin layer. The similar phenomenon was also observed in transmission electron microscope with accelerating voltage 120 kV [68]. The bilateral behaviour offers a possibility of new type of ionic memory, if a regulation method is utilized to control the growth and dissolution of Ag clusters, such as modification of electron beam intensity.
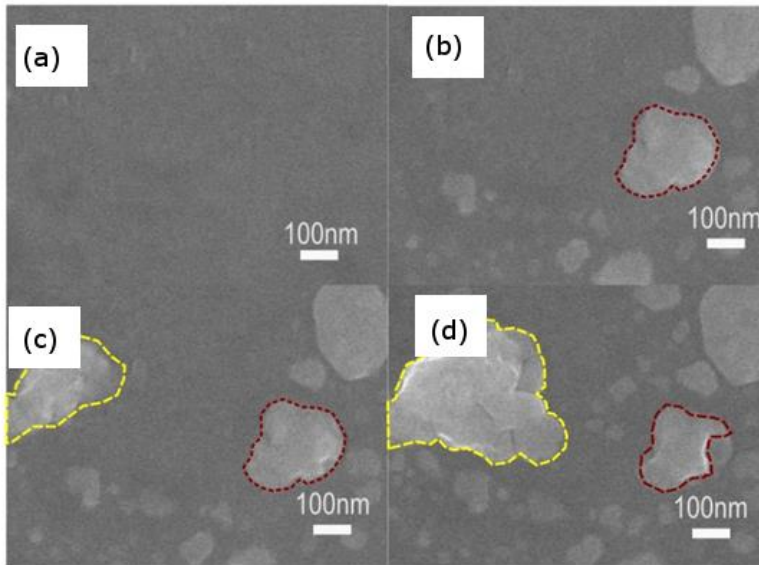
Figure 44: The selected SEM image (×100,000) of Ag clusters and Ag-rich regions; (a) 0 s, (b) 150 s, (c) 180 s, (d) 300 s.

Figure 45 shows the statistical data obtained from SEM image (Figure 44) with ×100,000 magnification. As the higher magnification was used, the exposure time was shortened to be 5 minutes, compared with 10 minutes in Figure 39. The number of clusters in Figure 42 (a) exhibits a saturation value, since 240 s. And their total number is below 10. The maximum size of clusters shows an increasing trend up to 500 nm, as shown in Figure 42 (b). The total process can be summarized by two parts: I) the nucleation of Ag embryos between 30 s and 240 s, and II) the growth in diameter after 30 s.
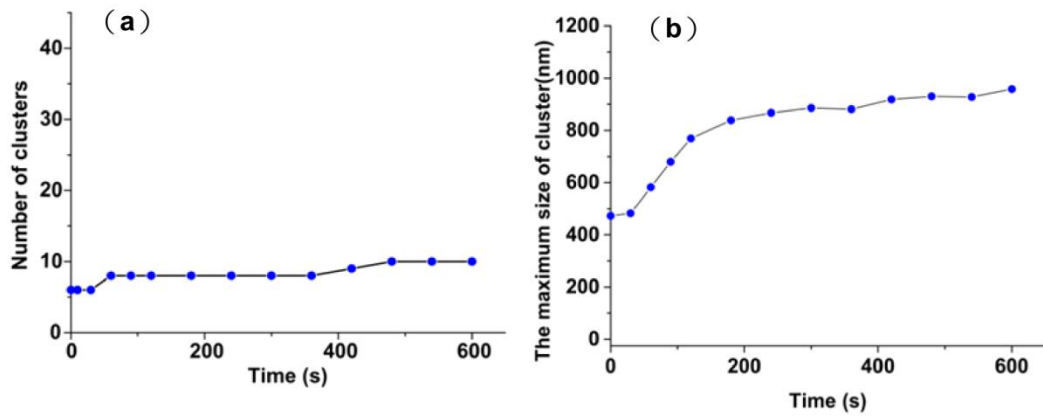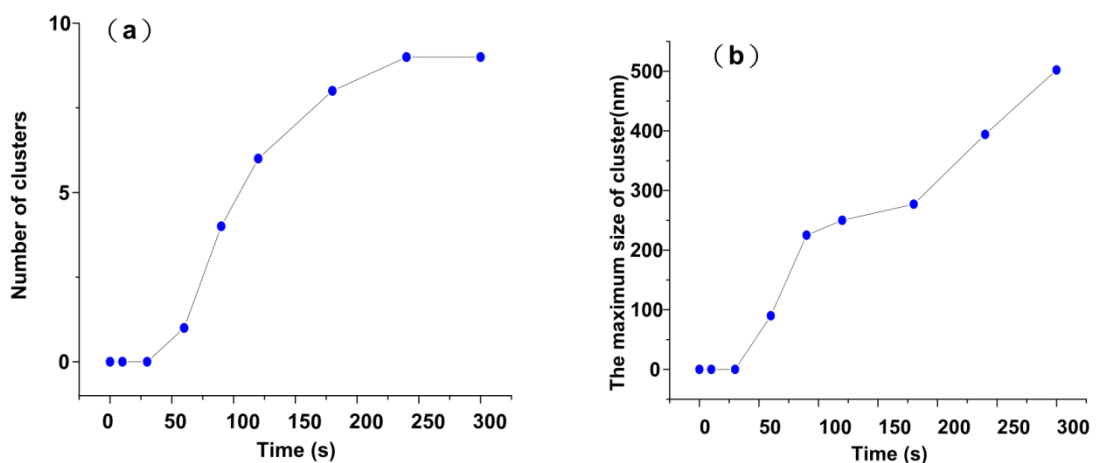

Figure 45: The statistical data obtained from SEM image with ×100,000 magnification: (a) The number of clusters developed with time per area of approx. 700× 700 nm^2 (b) The maximum size of clusters developed with time per area of approx. 700× 700 nm^2.

Figure 46 shows the SEM image of AsS_2/Ag bilayer prepared without photo doping, which was irradiated by electron beam at 5 kV at ×1000 magnification. The grey rectangle presents the irradiated region and the white background is the AsS_2 thin layer. It can be clearly found that no Ag particles were deposited on the top of the thin layer sample. Therefore, no electron beam induced Ag doping was existed. That might be explained by the nature of photo doping effect. The initial state of AsS_2 layer after deposition is the polymerized and relaxed in the photo doping process. It is a photochemistry process, involving both photo and thermal influence. Therefore, electron beam cannot induce the polymerization of the AsS_2 thin layer, which is properly the perquisite for Ag doping.
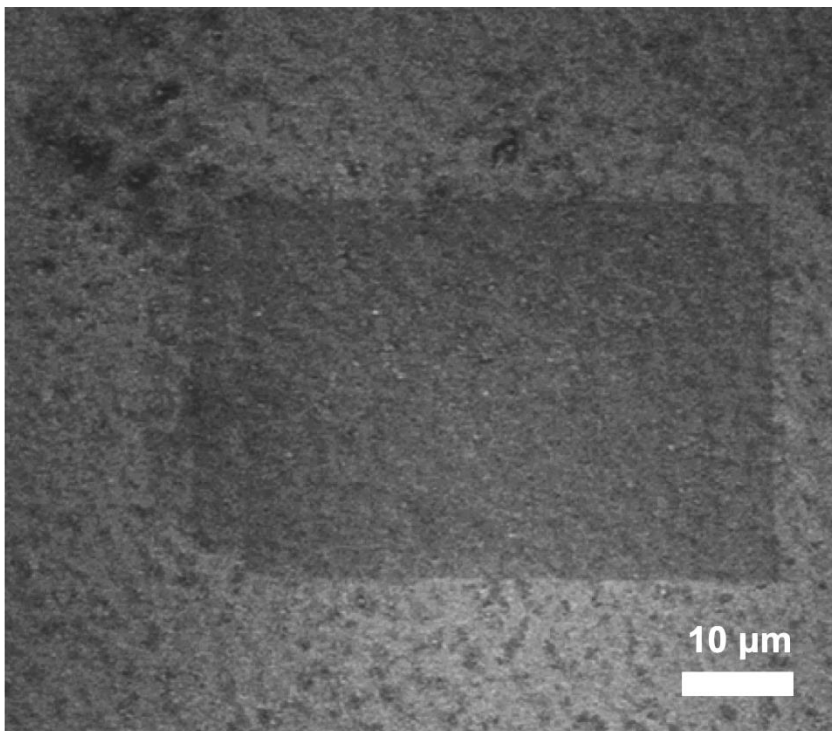
Figure 46: SEM image of AsS_2/Ag sample irradiated by electron beam at 5 kV at ×1,000 magnification.

5.3.4 Summary

In this chapter, we demonstrated a resistive switching measured with a needle contact. The cross section of thin layers was observed by SEM and the Ag filament was identified. In addition, an electric beam induced surface deposition was also discussed.

5.4 Tip (conductive AFM) geometry

5.4.1 Introduction

Conductive atomic force microscopy belongs to the group of scanning probe microscopy, which offers not only image of surface morphology but also the spread current map under bias. Therefore, the resistive switching can be studied via the biased AFM tip, which can be realized by either stationary or scanning mode. Stationary mode can be understood as biasing via immobile tip, which would output I-V curve. The biasing of scanning mode is done by mobile tip, taping the surface, which output is a spread current map. In our study, we adapted scanning mode, in order to obtain the distribution of conductive filament. The sample preparation is exactly the same as the needle contact geometry sample.

Morphology of the thin layers (cells) was investigated by a scanning electron microscope (JEOL JSM 7500F), and further analysed by ImageJ software. The resistive switching of the cells was evaluated by a conductive atomic force microscope (AFM Solver Pro M, NT-MDT; Russia) with a silicon probe coated with the Cr/Pt layer, scanning first from 10 mV to 100 mV and then from −10 mV to −100 mV with bias step 30 mV. The tapping mode was selected to investigate I) the in situ surface morphology of the memory cell, in particular volume changes and II) the spread currents. The screened area had a size of 3×3 μm^2. The optical images were measured by optical microscope (Olympus BX51), in which reflected mode and transmission mode can be selected. However, the measurement of chalcogenide thin layer, especially as-prepared Ag-doped thin layer, could be problematic, due to the photo induced phenomena. Moreover, focused light beam could induce surface oxidation, turning AsS_2 layer into poisonous As_2O_3-based oxides. In addition, the Ag doping could also happen during photo accumulation, in which yellow AsS_2 layer was switched into red $AgAsS_2$ thin layer.

Specifically, Ag deposition on to the surface is intrigued after photo doping, during prolonged illumination. Observation of resistive switching by conductive AFM is not a new topic [70]. Resistive switching in oxide and chalcogenide thin layer can be studied by conductive AFM. In general, there are two methods: I) scanning of specific area with different voltages by taping mode, II) another is applied voltage at a fixed point with a stationary tip.

The resistive switching scanning with a stationary tip was widely used [71]. As the small size of AFM tip (20–60 nm), the R_{ON} and R_{OFF} difference can be as high as the sample with electrode prepared photoresist lithography. The area after switching was taken for AFM scanning with tapping mode to find out the conductive region However, the leakage of current

for such mechanical contact is also very high, in creating Ag particles on the surface of thin layer.

In our case, we used area scanning with tapping mode to induce filament and dissolve filament. Spread current map and morphology map were recorded with changing of applied bias. As Ag ions were doped through photo doping, the sample can be influenced by the external illumination. Specifically, the photo induced electrons and holes at interface would affect the filament distribution.

5.4.2 The maps of surface morphology and distribution of spread current

Figure 47 shows the surface morphology of the cell. As one can see, the surface consists of Ag particles (with different dimensions) grown on the Ag_xAsS_2 layer by the OIDD process. Based on the particle size evaluation, shown in Figure 47 (a), it can be seen that number of surface particles decrease (from more than 30 to less than 5) with the increasing diameter of particles (from less than 200 nm to more than 650 nm). Moreover, the particles are uniformly distributed over the surface of whole cell. Figure 47 (b) shows an enlarged image of the Ag particles. From these observations, it can be deduced the Ag particles grow up with a different speed or different growth time upon the illumination (using OIDD). Figure 47(c) shows a scheme of the C-AFM measurement of the thin cells. The positive electrode consists of the Ag layer and the negative electrode consists of the C-AFM tip utilized for analysis.
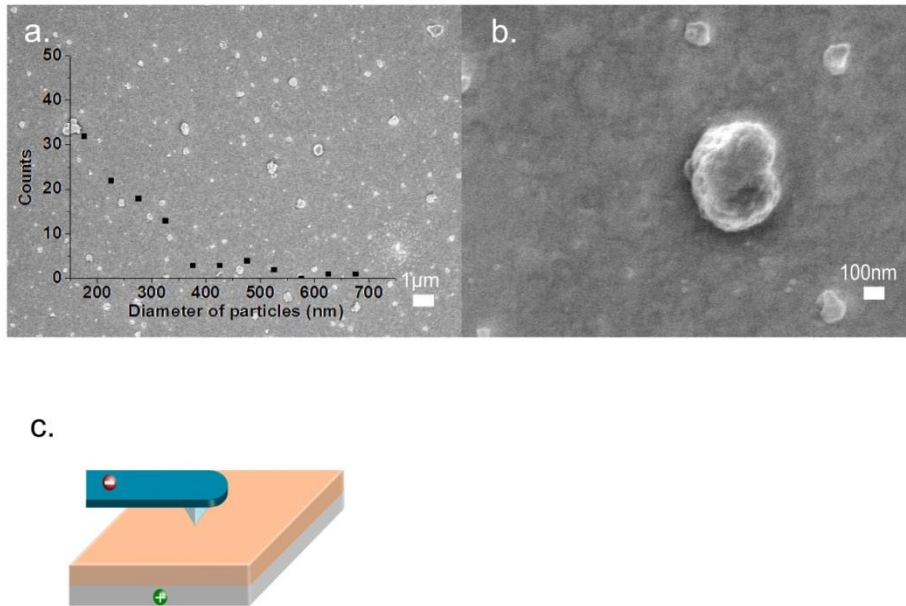
Figure 47: (a) SEM image of Ag particles grown on the Ag_xAsS_2 layer by OIDD (The inset shows the Ag particle size distribution on the layer), (b) an enlarged SEM image showing Ag particle in detail, (c) the scheme of experimental setup.

Figure 48 shows the optical image of the tip above the Ag doped AsS_2 thin layer before and after applied voltage. It is noticeable that the bias was applied in relative high and long time with stationary tip. And Ag precipitation was observed as branching structure, initiated from the AFM tip. That situation should be avoided by applying short pulse of bias and gradually increase the bias.
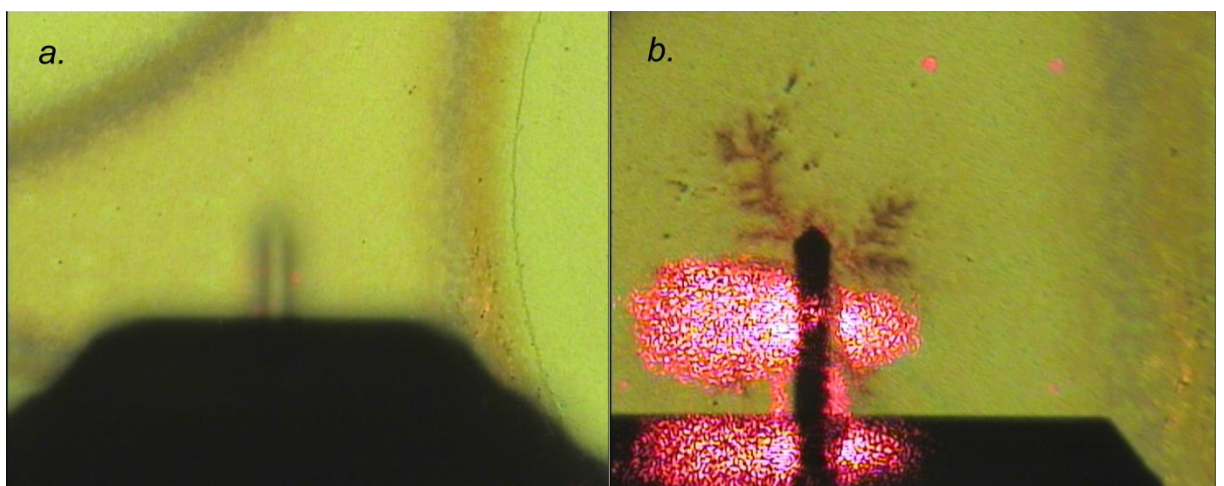
Figure 48: Optical image of conductive AFM and its tip, which shows tree branching after applied with 2.5 V for 1 second ((a) before voltage applied, (b) after voltage applied).

Figure 49 shows a sequence of topographical maps and spread current maps recorded on the surface of Ag_xAsS_2 in various periods of the switching cycle. In the 2D topological map shown in Figure 49 (a), it was recorded before any external bias was applied to the cell. Three extra-large spots can be distinguished that represent Ag particles created on the Ag_xAsS_2 layer by OIDD. The corresponding spread current map in Figure 49 (a) revealed an interesting phenomenon that can be entitled "inversed current flow". In this case, the current flows in the opposite direction (than expected considering the polarities given in Figure 49(c)) due to some kind of surface charge, in the same way as xerographic photoreceptor within coping machines [72].

Figure 49 (b) corresponds to the case, when a bias of 70 mV was applied to the cell. It can be seen that almost no volume change occurred under this bias. However, the corresponding spread current map shows an apparent current increase, compared with the map in Figure 49 (a), where current flows mainly around the Ag particles. The recorded current in this case stems from a number of trapped electrons due to the fact that the sample was exposed on a daily light for a short time between the OIDD process and the C-AFM measurement (to set up the tip). It is not yet a current that could be assigned to the initial stage of the filament growth.

Figure 49 (c) corresponds to the case, when a bias of 100 mV was applied to the cell. Compared with results of Figure 49 (a) and 49 (b), a whole range of new particles with different size appeared on the surface. In addition, the initial 3 spots were also expanded in size. In our opinion, these changes can be attributed to reduction of the Ag ions (from Ag_xAsS_2 layer) on the cells surface due to applied bias [73]. In addition, the current increased considerably compared to the 70 mV bias shown in Figure 49 (b). By comparison of maps in Figure 49 (c), one can see that the current flows not through the newly grown surface particles, but rather around. This is likely due to the fact, that at this surrounding area, newly grown Ag filaments are presented within the Ag_xAsS_2 layer. In other words, the current map shows dark regions exactly on the same areas, where particles are present.

Figure 49 (d) corresponds to the final step of the switching cycle, when a bias of −100 mV was applied on the cell. As once can see, most of particles (including those originally present on the surface prior to biasing) disappeared due to Ag oxidation to Ag^+ ions that dissolved into the Ag_xAsS_2 layer under the negative bias applied. The current map shows a dramatic decrease of the current (compared to Figure 49 (c)), presumably due to the dissolution of filaments.
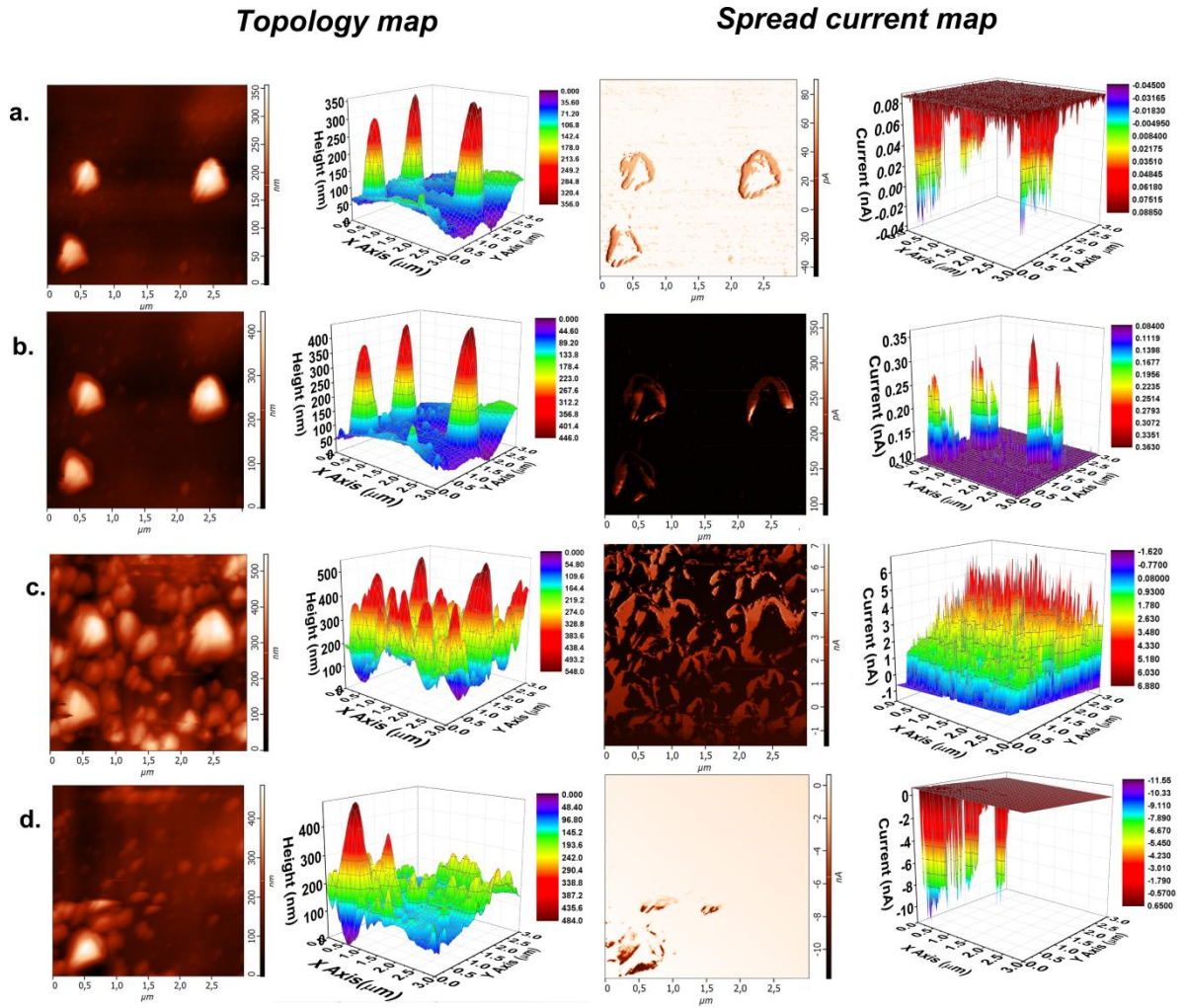
Figure 49: 2D and 3D topological maps (left column) and spread current maps (right column) of the Ag$_x$AsS$_2$ layer obtained under applied bias of (a) 0 mV, (b) 70 mV, (c) 100 mV, (d) −100 mV.

Figure 50 (a) plots the sum of currents (calculated from the data points in the spread current maps) as a function of the applied bias. In fact, the calculated values represent the total current that flowed through the whole selected geometrical area (3×3 μm^2) scanned by the C-AFM. Due to the relatively high degree of a noise throughout all corresponding maps, the currents smaller than 1 nA were not considered for the sum. However, the final current sums are specific enough to make some interesting conclusions. As it can be seen there is a current transition between 70 mV and 100 mV from approx. 10 nA to 1000 nA. This transition (in correlation with Figure 49) represents the Ag filament formation within the Ag$_x$AsS$_2$ layer. The current drops at −10 mV due to the sudden decrease in the applied bias. Upon further biasing to negative bias, the Ag filaments begin to dissolve. Finally, at −100 mV, the current

starts to decay, due to rupture of the conductive filaments. It is worth to mention that the resistance at −100 mV cannot be recovered to the initial resistance at 0 mV, which is caused by an incomplete dissolution of thick filaments, as indicated in the Figure 3 (a).

Figure 50 (b) plots the volume change of Ag_xAsS_2 layer, derived from the topological maps obtained by C-AFM measurements, as a function of applied bias. Compared to the current data, the topological data were much less noisy and the overall noise had a very minor influence on the overall sum. As discussed above, there is not direct relationship of the Ag particles and conductive filament within the Ag_xAsS_2 layer, since the current has not flowed through these particles. However, the general trend of the volume change during biasing on the cell fits very well with the current changes.
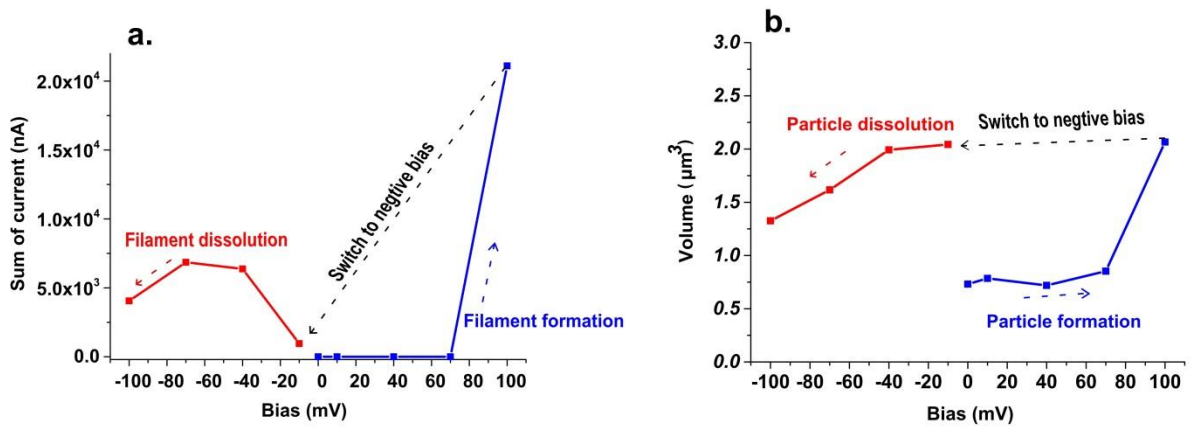
Figure 50: (a) The sum of current flowing through the thin layer, (b) the volume change of thin layer. The blue and red lines represent currents recorded under positive and negative bias, respectively (arrow indicates the direction of bias).

5.4.3 The explanation of data

In fact, an applied bias can cause the Ag^+ ion to be reduced from the Ag_xAsS_2 layer either on its surface or within its internal volume, resulting in Ag particles or Ag filaments, respectively. The Ag particles on surface of the layer are themselves likely conductive, however, the current does not have a tendency to flow through them. In contrary, the conductive regions shown in spread current maps suggest the presence of conductive filaments (in the Ag_xAsS_2 layer), presented in the Ag_xAsS_2 layer around Ag particles.

Therefore, a model explaining the mechanism of the Ag particle and Ag filament formation was proposed in Figure 51, based on the distribution (and interaction) of charge carriers and Ag ions within the Ag_xAsS_2 layer. It is a graphical representation of the reduction of Ag ions

into particles and filaments during the illumination (OIDD) [74] (Figure 51(a) and 51(b)) and C-AFM biasing (Figure 4 (c) and 4 (d)), respectively. Under illumination, the charge carriers would be generated strongly at the surface. Due to higher mobility of holes in the Ag_xAsS_2 layer, the holes diffuse into the interior of thin layer, while the less mobile electrons are aligned at the surface [75]. Electrons and holes form a double layer there, by which the Ag ions are separated away from the uppermost part of surface, as depicted in Figure 51 (a). The Ag ions diffuse through the region of accumulated holes and the surface residual electrons lead to the reduction of Ag ions on the surface, as described in Figure 51 (b). As explained above, only Ag particles are formed under illumination (OIDD). Figure 51 (c) exhibits the possible distribution (in the area without Ag particles) of carriers-rich region (position 1) and Ag ions-rich region (position 2) at the interface after illumination (OIDD). As depicted in Figure 51 (d), after biasing the layer, the repulsion between holes and Ag ions takes place. As a result, the reduction of Ag ions (from Ag species forming filaments) occurs within the internal volume of Ag_xAsS_2 layer at position 1, in comparison with surface reduction (forming Ag particles) at position 2. In addition, the mechanism of filament formation around photo induced Ag particle is the same as described above, due to the existence of carrier-rich region. This is in line with observations shown in Figure 49 (c), that the Ag ions-rich regions are surrounded by the carriers-rich regions. In other words, the Ag particles are located between the conductive regions (corresponding to Ag filaments) in the spread current maps.

Figure 51: The mechanism of Ag particle and filament formation on and within Ag_xAsS_2 layer; (a) the initial formation of electron-hole double layer and diffusion of Ag ions under illumination, (b) the reduction of Ag ions by surface electrons and followed Ag particles
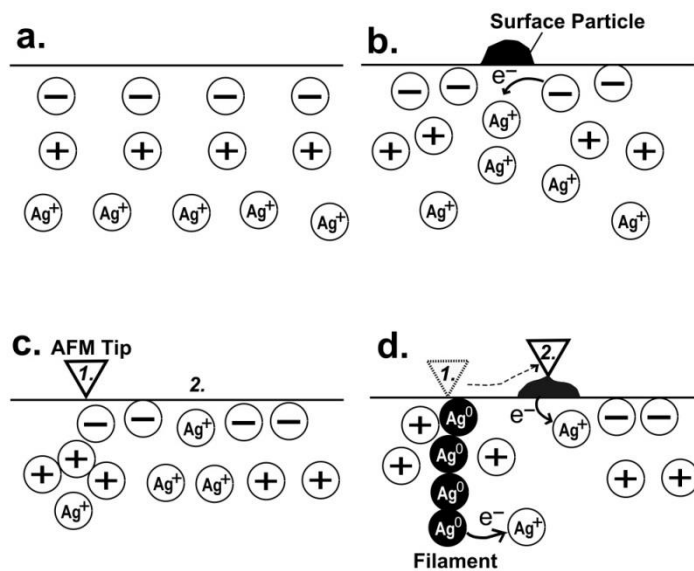
formation under illumination, (c) the initial state of C-AFM scans after illumination. At position 1, there is carrier-rich region layer blocking the diffusion of Ag ions; at positon 2, the Ag ions reach the surface thin layer, (d) the filament and surface particle formations at position 1 and 2.

5.4.4   Summary

In this chapter, we reported an investigation of the resistive switching by C-AFM on Ag_xAsS_2 layer. The current and volume changes within the Ag_xAsS_2 layer occurred under a bias, due to the growth of filaments and formation of Ag particles, respectively. The sum of current and volume are presented with similar trend. In addition, it turned out that the Ag particles can be created either by an external bias or upon an illumination (OIDD), while Ag filament formation can only be induced under C-AFM bias. The surface morphology map and spread current map from conductive AFM shows an inversed distribution in which current did not flow through particles but the boundaries of particles. Therefore, a model with distribution of surface carriers was put forward. The electrons and holes can be formed at the surface of chalcogenide thin layer, during the exposure of external light and the holes are more mobile than the electrons [75]. According to the proposed model, it is assumed that a double layer formed during the illumination. The force of repulsion from Ag ions and carries is taken into consideration in which the electrons attract the Ag ions to the surface and reduce Ag ions into Ag particles under illumination. Meanwhile, holes repel the Ag ions from the migration, due to electric polarity. Under the applied bias, the Ag ions are migrated to the top of surface. However, as existence of holes layer, the migration of Ag ions are retardant and pushed holes the surrounding area, at which particles are formed at the top of surface and filaments are formed across the holes barrier. The presented results could be helpful for a better understanding of the resistive switching mechanism.

5.5   Via-hole geometry

Via-hole geometry is widely used in the field of RRAM, for its simplicity to be integrated. Many memory circuits are fabricated according to via-hole geometry, for instance 1T1R [76], 1D1R [53] and 1BJT1R [77], which shows great potential to be commercialized. In our case, the fabrication started from the deposition of Ti adhesion layer onto SiO_2 substrate, and a layer of Pt layer eas followed as the bottom electrode. The SiO_2 layer was deposited by PECVD as a barrier layer, and then etched into graphic picture during photoresist lithography process. The electrolyte and top electrode were deposited normally as the other geometries, as

shown in Figure 52.
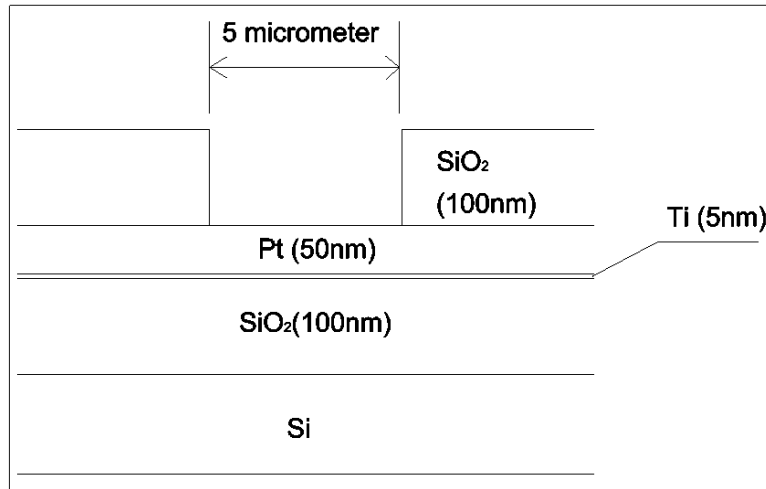
Figure 52: The profile dimension of fabricated device after photoresist lithography.

Before deposition of chalcogenide GeSe$_2$ thin layer, the sample was treated in heated acetone and propanol for 15 minutes to completely remove the photoresist from the sample surface. It is noticeable to mention the sample is vulnerable to any contamination, therefore all the operation should be done in clean bench. The Ag was doped into GeSe$_2$ thin layer by photo doping: Firstly, an ultrathin layer (10 nm) was deposited onto the top of GeSe$_2$ thin layer, then the sample was illuminated by UV light source ($\lambda = 400$ nm) in inert environment until all the Ag doped into chalcogenide thin layer. The ultrathin Ag layer was utilized in this step, because of its transparency to UV light. The Ag electrode was the last deposition, which 100 nm was achieved to ensure the sufficient conductivity and stable Ag source for device.

It can be seen from Figure 53 that the I-V curves in sample with via-hole geometry. The scanning range is between 0.4 and −0.4 V, and current limit is 1×10^{-5} A. It shows 5th order R$_{ON}$ and R$_{OFF}$ difference, which is the highest among five geometries. In contrast with Figure 34, the sample in via-hole geometry owns lower threshold voltage and current limit, which exhibits the miniature of device in photoresist lithography. In addition, the buffer or barrier layer is not needed in via-hole sample, in comparison with crossbar geometry and the dimension of electrode can be much smaller, in comparison with spot geometry, which is much convenient to be commercialized [8].
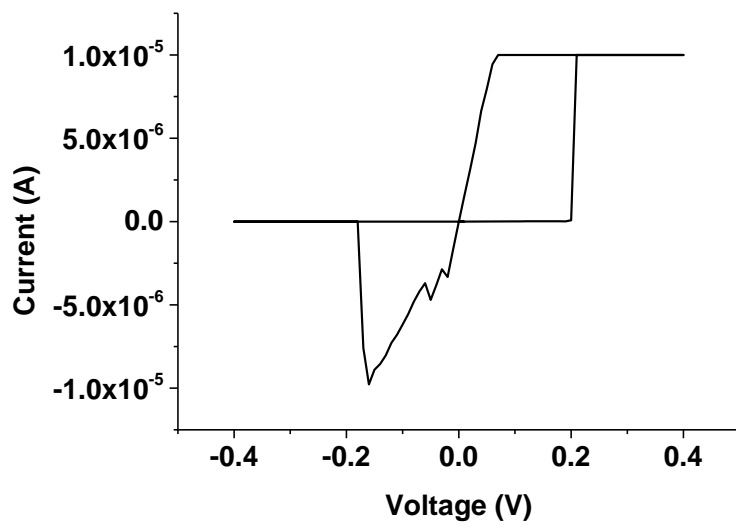
Figure 53: I-V curve in sample (Pt/AgGeSe$_2$/Ag) with via-hole geometry.

6 Conclusion of thesis

In this thesis, resistive switching devices were fabricated with ionic Ag-doped chalcogenide thin film. Five different geometries were discussed in the context.

The resistive switching is accounted for the material resistance in variation with external voltage. The variation of resistance commonly results in two resistance states, which has been discovered in semiconductor, insulator, and solid state electrolyte. In our study, Ag ions doped chalcogenide was selected as the electrolyte.

Five geometries of memory cells were discussed in the context of thesis, which are spot geometry, crossbar geometry, needle contact geometry, tip (conductive AFM) geometry and via-hole geometry. According to the properties of electrodes, those can be divided by two types: sample with fixed electrode and samples with floated electrode. Fixed electrodes were utilized for device study, while floated electrodes were designed for investigating the switching property of material.

The fixed electrodes were prepared via thermal evaporation or magnetron sputtering and the outline of electrodes were defined by stainless steel mask or photoresist lithography. The dimension of electrode in crossbar geometry is 0.1 mm, in contrast to 5 µm in via-hole geometry. Furthermore, the I-V curve of via-hole geometry exhibits lower compliance current and SET voltage than that with the crossbar geometry. Therefore, the via-hole geometry is promising to be commercialized in the future.

Although the study of resistive switching has been carried on over half century, the mechanism is still on debate. Up to now, the conductive filament model has been the most popular. Therefore, the observation of filament is of great importance for learning the physical property of resistive switching.

The filament observation was carried out by SEM and conductive AFM. In order to observe the cross-sectional view, the sample was cut mechanically. With the secondary electron mode of SEM, several filaments can be seen, which is embedded in the thin film matrix. In addition, due to the existence of electron beams, the Ag particles were deposited onto the top of thin film. The top view of filaments was obtained by conductive AFM.

In summary, the resistive switching Ag doped chalcogenide electrolyte was discussed in the content with five different geometries. The filament was observed either by SEM or AFM, offering fruitful information for future investigation.

7   Reference

[1]   Von Neumann architecture, Wikipedia. (access data: 14 May 2017). https://en.wikipedia.org/wiki/Von_Neumann_architecture.

[2]   Wikipedia, Dynamic random-access memory, (access data: 14 May 2017). https://en.wikipedia.org/wiki/Dynamic_random-access_memory.

[3]   Diffen, RAM vs. ROM, (n.d.). http://www.diffen.com/difference/RAM_vs_ROM.

[4]   J.F. Scott, Ferroelectric memories, Phys. World. 8 (1995) 46–50. doi:10.1126/science.246.4936.1400.

[5]   R.J. Lipton, J.S. Sandberg, Pram: A scalable shared memory, Princent. Univ. (1988) 13.

[6]   T.M. Maffitt, J.K. DeBrosse, J. a. Gabric, E.T. Gow, M.C. Lamorey, J.S. Parenteau, et al., Design considerations for MRAM, IBM J. Res. Dev. 50 (2006) 25–39. doi:10.1147/rd.501.0025.

[7]   X. Dong, X. Wu, G. Sun, Y. Xie, H. Li, Y. Chen, Circuit and microarchitecture evaluation of 3D stacking magnetic RAM (MRAM) as a universal memory replacement, in: Proc. - Des. Autom. Conf., 2008: pp. 554–559. doi:10.1109/DAC.2008.4555878.

[8]   R. Waser, M. Aono, Nanoionics-based resistive switching memories., Nat. Mater. 6 (2007) 833–840. doi:10.1038/nmat2023.

[9]   T. Yanagida, K. Nagashima, K. Oka, M. Kanai, A. Klamchuen, B.H. Park, et al., Scaling Effect on Unipolar and Bipolar Resistive Switching of Metal Oxides, Sci. Rep. 3 (2013) 1657. doi:10.1038/srep01657.

[10]   F. Pan, C. Chen, Z. Wang, Y. Yang, J. Yang, F. Zeng, Nonvolatile Resistive Switching Memories-Characteristics, Mechanisms and Challenges, Prog. Nat. Sci. Mater. Int. 20 (2010) 1–15. doi:10.1016/S1002-0071(12)60001-X.

[11]   D.J. Wouters, R. Waser, M. Wuttig, Phase-Change and Redox-Based Resistive Switching Memories, Proc. IEEE. 103 (2015) 1274–1288. doi:10.1109/JPROC.2015.2433311.

[12]   G.H. Oh, Y.L. Park, J.I. Lee, D.H. Im, J.S. Bae, D.H. Kim, et al., Parallel multi-confined (PMC) cell technology for high density MLC PRAM, 2009 Symp. VLSI Technol. 4 (2009) 220–221.

[13]   P.Dorion, O.Cueto, M.Reyboz, Simulation of CBRAM devices with the level set method, in: Simul. Semicond. Process. Devices, Glasgow, 2013: pp. 340 – 343. doi:10.1109/SISPAD.201

3.6650644.

[14]   K. Terabe, T. Hasegawa, T. Nakayama, M. Aono, Quantized conductance atomic switch., Nature. 433 (2005) 47–50. doi:10.1038/nature03190.

[15]   Y. Hirose, H. Hirose, Polarity-dependent memory switching and behavior of Ag dendrite in Ag-photodoped amorphous As_2S_3 films, J. Appl. Phys. 47 (1976) 2767–2772. doi:10.1063/1.322942.

[16]   F. Pan, S. Gao, C. Chen, C. Song, F. Zeng, Recent progress in resistive random access memories: Materials, switching mechanisms, and performance, Mater. Sci. Eng. R Reports. 83 (2014) 1–59. doi:10.1016/j.mser.2014.06.002.

[17]   S. Kasap, P. Capper, Handbook of Electronic and Photonic Materials, Springer, 2006. doi:10.1007/978-0-387-29185-7.

[18]   N.M. White, J.D. Turner, Thick-film sensors: Past, present and future, Meas. Sci. Technol. 8 (1997) 1–20. doi:10.1088/0957-0233/8/1/002.

[19]   M.N. Kozicki, A. Tempe, M. Balakrishnan, Programmable metallization cell memory based on Ag-Ge-S and Cu-Ge-S solid electrolytes, in: Non-Volatile Mem. Technol. Symp., 2005: pp. 7–89. doi:10.1109/NVMT.2005.1541405.

[20]   J. Kolar, J.M. Macak, K. Terabe, T. Wagner, Down-scaling of resistive switching to nanoscale using porous anodic alumina membranes, J. Mater. Chem. C. 2 (2014) 349. doi:10.1039/c3tc31969e.

[21]   X. Guo, C. Schindler, S. Menzel, R. Waser, Understanding the switching-off mechanism in Ag^+ migration based resistively switching model systems, Appl. Phys. Lett. 91 (2007). doi:10.1063/1.2793686.

[22]   C. Schindler, S. Chandran Puthen Thermadam, R. Waser, M. N. Kozicki, Bipolar and Unipolar Resistive Switching in Cu-Doped SiO_2, IEEE T-ED. 54 (2007) 2762–2768. doi:10.1109/TED.2007.904402.

[23]   C. Schindler, K. Szot, S. Karthäuser, R. Waser, S. Karthauser, R. Waser, Controlled local filament growth and dissolution in Ag-Ge-Se, Phys. Status Solidi-Rapid Res. Lett. 2 (2008) 129–131. doi:10.1002/pssr.200802054.

[24]   M. Balakrishnan, M. Mitkova, S. C. P. Thermadam, M.N. Kozicki, A low power non-volatile memory element based on copper in deposited silicon oxide, in: Proc. 2006 Non-Volatile

Mem. Technol. Symp., 2006: pp. 104–110.

[25]   M.A. N. Banno, T. Sakamoto, T. Hasegawa, K. Terabe, Effect of ion diffusion on switching voltage of solid-electrolyte nanometer switch, Jap. Appl. Phys. 45 (2006) 3666–3668. doi: 10.1143/JJAP.45.3666

[26]   R. Waser, R. Dittmann, C. Staikov, K. Szot, Redox-based resistive switching memories nanoionic mechanisms, prospects, and challenges, Adv. Mater. 21 (2009) 2632–2663. doi:10.1002/adma.200900375.

[27]   S.C. Chae, J.S. Lee, S. Kim, S.B. Lee, S.H. Chang, C. Liu, et al., Random circuit breaker network model for unipolar resistance switching, Adv. Mater. 20 (2008) 1154–1159. doi:10.1002/adma.200702024.

[28]   D.S. Jeong, H. Schroeder, U. Breuer, R. Waser, Characteristic electroforming behavior in Pt/ TiO$_2$/Pt resistive switching cells depending on atmosphere, J. Appl. Phys. 104 (2008) 100– 107. doi:10.1063/1.3043879.

[29]   J. Joshua Yang, F. Miao, M.D. Pickett, D.A. Ohlberg, D.R. Stewart, C.N. Lau, et al., The mechanism of electroforming of metal oxide memristive switches., Nanotechnology. 20 (2009) 215201. doi:10.1088/0957-4484/21/33/339803.

[30]   K.M. Kim, B.J. Choi, S.J. Song, G.H. Kim, C.S. Hwang, Filamentary Resistive Switching Localized at Cathode Interface in NiO Thin Films, J. Electrochem. Soc. 156 (2009) G213. doi:10.1149/1.3240201.

[31]   K. Nagashima, T. Yanagida, M. Kanai, U. Celano, Carrier type dependence on spatial asymmetry of unipolar resistive switching of metal oxides, Appl. Phys. Lett. 103 (2013). doi: dx.doi.org/10.1063/1.4826558.

[32]   J.Y. Chen, C.L. Hsin, C.W. Huang, C.H. Chiu, Y.T. Huang, S.J. Lin, et al., Dynamic evolution of conducting nanofilament in resistive switching memories, Nano Lett. 13 (2013) 3671–3677. doi:10.1021/nl4015638.

[33]   Z.U. Borisova, Glassy semiconductors, Plenum Press, New York,USA, 1981.

[34]   S.R. Elliott, Physics of amorphous materials, 1st ed., Longman Group Ltd., London, 1984.

[35]   N. Mehta, Applications of chalcogenide glasses in electronics and optoelectronics: A review, J. Sci. Ind. Res. (India). 65 (2006) 777–786.

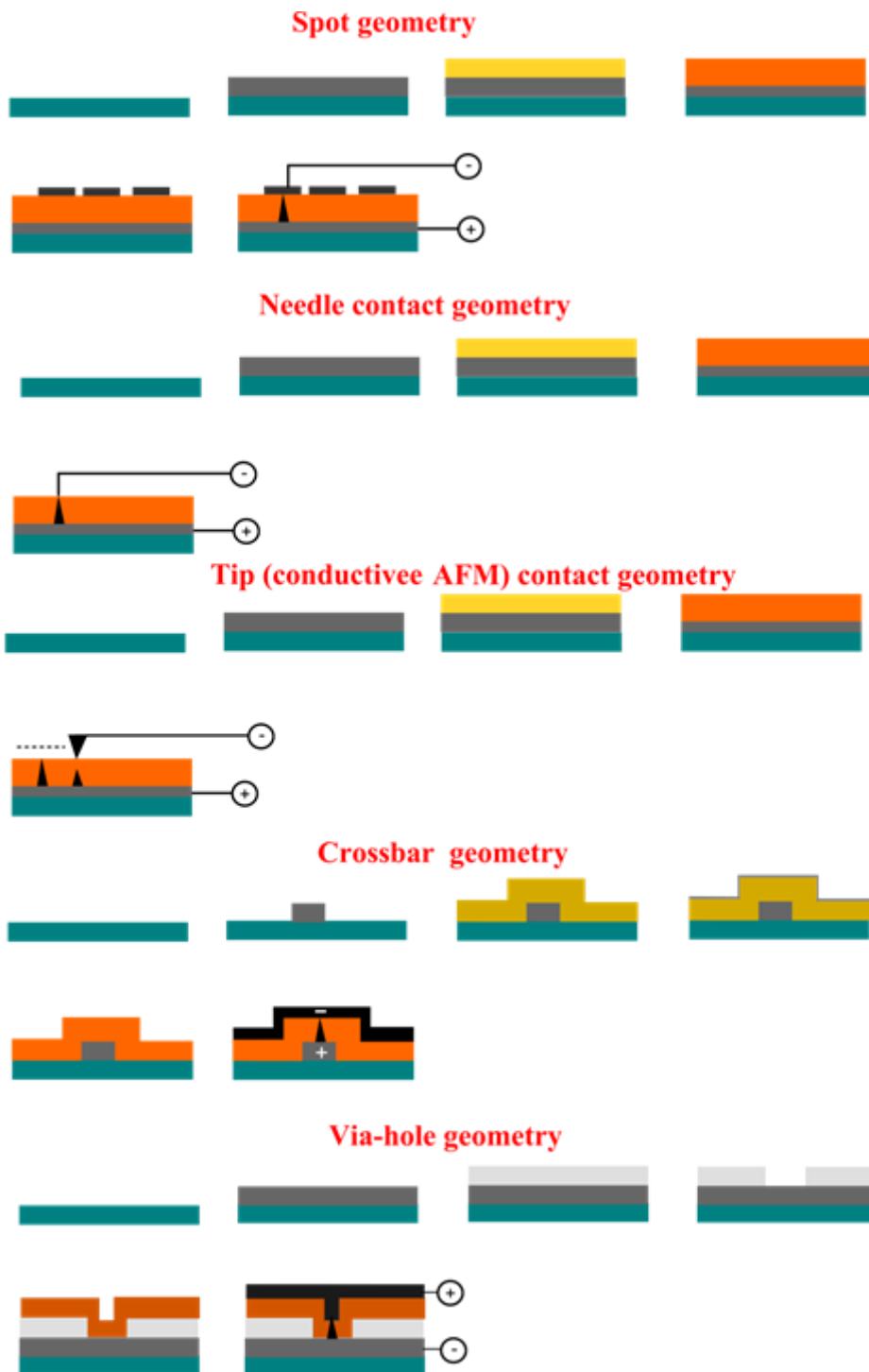[36]   M.T. Kostyshin, E.V. Mikhaylovskaya, P.E. Romanenko, Photographic-Sensitivity Effect in

Thin Semiconducting Films on Metal Substrates, Sov. Phys. Solid State. 8 (1966) 451 452.

[37] A.V. Kolobov, S.R. Elliot, Photodoping of amorphous chalcogenides by metals, Adv. Phys. 40 (1991) 625–684.

[38] A.E. Owen, A.P. Firth, P.J.S. Ewen, Photoinduced structural and physicochemical changes in amorphous-chalcogenide semiconductors, Philos. Mag. B. 52 (1985) 347–362.

[39] T. Kawaguchi, K. Tanaka, S.R. Elliott, Photoinduced and electron-beam phenomena in Ag rich amorphous chalcogenide semiconductors, in: Handb. Adv. Electron. Photonic Mater. Devices, 2001: pp. 92–117.

[40] M.S. Ailavajhala, T. Nichol, Y. Gonzalez-Velo, H.J.B. Christian D. Poweleit, Thin Ge–Se films as a sensing material for radiation doses, Phys. Status Solidi. 251 (2013) 1347–1353. doi: 10.1002/pssb.201350188.

[41] S. Dietrich, M. Angerbauer, M. Ivanov, D. Gogl, H. Hoenigschmid, M. Kund, et al., A nonvolatile 2-Mbit CBRAM memory core featuring advanced read and program control, IEEE J. Solid-State Circuits. 42 (2007) 839–845. doi:10.1109/JSSC.2007.892207.

[42] M.N. Kozicki, C. Gopalan, M. Balakrishnan, M. Mitkova, A Low-Power Nonvolatile Switching Element Based on Copper-Tungsten Oxide Solid Electrolyte, IEEE Trans. Nanotechnol. 5 (2006) 535 – 544.

[43] J.Z. Liu, P.C. Taylor, A general structural model for semiconducting glasses, Solid State Commun. 70 (1989) 81–85.

[44] A. Pradel, N. Frolet, M. Ramonda, A. Piarristeguy, M. Ribes, Bipolar resistance switching in chalcogenide materials, Phys. Status Solidi. 208 (2011) 2303–2308. doi:10.1002/pssa.201000 767.

[45] R. Soni, P. Meuffels, A. Petraru, M. Weides, C. Kugeler, R. Waser, et al., Probing Cu doped $Ge_{0.3}Se_{0.7}$ based resistance switching memory devices with random telegraph noise, J. Appl. Phys. 107 (2010) 1–4. doi:10.1063/1.3291132.

[46] C. Schindler, Resistive switching in electrochemical metallization memory cells, Technischen Hochschule Aachen, 2009.

[47] C.J. Kim, S.G. Yoon, K.J. Choi, S.O. Ryu, S.M. Yoon, N.Y. Lee, et al., Characterization of silver-saturated Ge-Te chalcogenide thin films for nonvolatile random access memory, J. Vac. Sci. Technol. B. 24 (2006) 721–724. doi: 10.1116/1.2180260.

[48]   H. Lv, H. Wan, T. Tang, Improvement of resistive switching uniformity by introducing a thin GST interface layer, IEEE Electron Device Lett. 31 (2010) 978–980. doi:10.1109/LED.2010. 2055534.

[49]   J.E. Green, J.W. Choi, A. Boukai, Y. Bunimovich, E. Johnston-Halperin, E. DeIonno, et al., A 160-kilobit molecular electronic memory patterned at 10(11) bits per square centimetre., Nature. 445 (2007) 414–417. doi:10.1038/nature05462.

[50]   A. Beck, J.G. Bednorz, C. Gerber, C. Rossel, D. Widmer, Reproducible switching effect in thin oxide films for memory applications, Appl. Phys. Lett. 77 (2000) 139. doi:10.1063/1.126902.

[51]   H.S. Yoon, I.-G. Baek, J. Zhao, H. Sim, M.Y. Park, H. Lee, et al., Vertical cross-point resistance change memory for ultra-high density non-volatile memory applications, 2009 Symp. VLSI Technol. (2009) 26–27.

[52]   A. Flocke, T.G. Noll, Fundamental analysis of resistive nanocross- bars for the use in hybrid nano/CMOS-memory, in: Proc. 33rd ESSCIRC, 2007: pp. 328–331.

[53]   M.J. Lee, Y. Park, B.S. Kang, S.E. Ahn, C. Lee, K. Kim, et al., 2-Stack ID-IR cross-point structure with oxide diodes as switch elements for high density resistance RAM applications, Tech. Dig. - Int. Electron Devices Meet. IEDM. (2007) 771–774. doi:10.1109/IEDM.2007.4419 061.

[54]   Z. Zhang, Y. Wu, H.P. Wong, S.S. Wong, Nanometer-Scale HfO$_x$ RRAM, IEEE Electron Device Lett. 34 (2013) 1005–1007. doi:10.1109/LED.2013.2265404.

[55]   M. Liu, New resistive switching technology, 1st ed., science press, Beijing, 2014.

[56]   Y. Yang, P. Gao, S. Gaba, T. Chang, X. Pan, W. Lu, Observation of conducting filament growth in nanoscale resistive memories, Nat. Commun. 3 (2012) 732. doi:10.1038/ncomms1737.

[57]   C. Sang Jun, P. Gyeong Su, K. Ki Hong, C. Soohaeng, In Situ Observation of Voltage-Induced Multilevel Resistive Switching in Solid Electrolyte Memory, Adv. Mater. 23 (2011) 3272–3277.

[58]   Y. Dong, G. Yu, M.C. McAlpine, W. Lu, C.M. Lieber, Si/a-Si core/shell nanowires as nonvolatile crossbar switches, Nano Lett. 8 (2008) 386–391. doi:10.1021/nl073224p.

[59]   K. Nagashima, T. Yanagida, K. Oka, M. Taniguchi, T. Kawai, J.S. Kim, et al., Resistive switching multistate nonvolatile memory effects in a single cobalt oxide nanowire, Nano Lett.

10 (2010) 1359–1363. doi:10.1021/nl9042906.

[60] S. Lee, J. Lee, J. Park, Y. Choi, K. Yong, Resistive switching WO_x-Au core-shell nanowires with unexpected nonwetting stability even when submerged under water, Adv. Mater. 24 (2012) 2418–2423. doi:10.1002/adma.201200068.

[61] L. Si-Hoon, L. Jang-Sik, Highly scalable resistive switching memory cells using pore-size-controlled nanoporous alumina templates, J. Mater. Chem. 22 (2012) 1852–1861. doi:1852-1861.

[62] Reference Manual, 2600s-901-01 Rev.B. (access data: 14 May 2017). http://www.ece.uprm.edu/~etclab/resources/equipment/keithley2612/2600series_referencemanual.pdf.

[63] JSM-7500F Field Emission Scanning Electron Microscope, (access data: 14 May 2017). http://www.jeol.co.jp/en/products/detail/JSM-7500F.html.

[64] Solver PRO M, (access data: 14 May 2017). http://amnol.usv.ro/DOC/AFM.pdf.

[65] Y.L. Song, Y. Liu, Y.L. Wang, M. Wang, X.P. Tian, L.M. Yang, et al., Low reset current in stacked AlO_x/WO_x resistive switching memory, IEEE Electron Device Lett. 32 (2011) 1439–1441. doi:10.1109/LED.2011.2162055.

[66] C. Schindler, I. Valov, R. Waser, Faradaic currents during electroforming of resistively switching Ag-Ge-Se type electrochemical metallization memory cells., Phys. Chem. Chem. Phys. 11 (2009) 5974–5979. doi:10.1039/b901026b.

[67] S. Ambrogio, S. Balatti, S. Choi, D. Ielmini, Impact of the mechanical stress on switching characteristics of electrochemical resistive memory, Adv. Mater. 26 (2014) 3885–3892. doi:10.1002/adma.201306250.

[68] J.S. Romero, A.J. Fitzgeral, M.J. Rose, transmission electron microscope study of metal/chalcogenide amorphous thin films, Appl. Surf. Sci. 234 (2004) 369–373. doi:10.1016/j.apsusc.2004.05.039.

[69] M. Barczewski, D. Matykiewicz, J. Andrzejewski, Effect of heterogeneous nucleation on isotactic polypropylene-polyoxymethylene blends properties and miscibility, Macromol. Res. 23 (2015) 850–860. doi:10.1007/s13233-015-3117-y.

[70] B. Zhang, P. Kutalek, P. Knotek, L. Hromadko, J.M. Macak, T. Wagner, Investigation of the resistive switching in Ag_xAsS_2 layer by conductive AFM, Appl. Surf. Sci. 382 (2016) 336–340. doi:10.1016/j.apsusc.2016.04.152.

[71] P. Bousoulas, J. Giannopoulos, K. Giannakopoulos, P. Dimitrakis, D. Tsoukalas, Memory programming of TiO_{2-x} films by Conductive Atomic Force Microscopy evidencing filamentary resistive switching, Appl. Surf. Sci. 332 (2015) 55–61. doi:10.1016/j.apsusc.2015.01.133.

[72] D.M. Pai, B.E. Springett, Physics of electrophotography, Rev. Mod. Phys. 65 (1993) 163–211. doi:10.1103/RevModPhys.65.163.

[73] M.N. Kozicki, C. Ratnakumar, M. Mitkova, Electrodeposit Formation in Solid Electrolytes, 2 006 7th Annu. Non-Volatile Mem. Technol. Symp. (2006). doi:10.1109/NVMT.2006.378888.

[74] V. Peřina, T. Wágner, M. Krbal, M. Frumar, RBS in situ studies of the kinetics of optically-induced diffusion of Ag in vacuum evaporated films with composition of $As_{33}S_{67}$, Nucl. Instruments Methods Phys. Res. Sect. B Beam Interact. with Mater. Atoms. 249 (2006) 352–354. doi:10.1016/j.nimb.2006.04.026.

[75] A. V. Kolobov, On the origin of p-type conductivity in amorphous chalcogenides, J. Non. Cryst. Solids. 198-200 (1996) 728–731. doi:10.1016/0022-3093(96)00119-6.

[76] M. Wang, W.J. Luo, Y.L. Wang, L.M. Yang, W. Zhu, P. Zhou, et al., A novel Cu_xSi_yO resistive memory in logic technology with excellent data retention and resistance distribution for embedded applications, in: Dig. Tech. Pap. - Symp. VLSI Technol., 2010: pp. 89–90. doi:10.1109/VLSIT.2010.5556182.

[77] M.F. Chang, C.C. Kuo, S.S. Sheu, C.J. Lin, Y.C. King, F.T. Chen, et al., Area-efficient embedded resistive RAM (ReRAM) macros using logic-process vertical-parasitic-BJT (VPBJT) switches and read-disturb-free temperature-aware current-mode read scheme, IEEE J. Solid-State Circuits. 49 (2014) 908–916. doi:10.1109/JSSC.2013.2297417.

8 Graphic illustration of sample preparation

Spot geometry

Needle contact geometry

Tip (conductivee AFM) contact geometry

Crossbar geometry

Via-hole geometry

Spot geometry: 1. Clean SiO_2 glassy substrate 2. deposition of Ag electrode 3.deposition of AsS_2 chalcogenide layer 4. photo diffusion and photo dissolution process induced by mercury lamp 5. deposited Al electrodes 6. filament formation under bias.

Needle contact geometry: 1. Clean SiO_2 glassy substrate 2. deposition of Ag electrode 3. the deposition of AsS_2 chalcogenide layer 4. photo diffusion and photo dissolution process induced by mercury lamp 5. filament formation under bias from pin electrode.

Tip (conductive AFM) contact geometry: 1. Clean SiO_2 glassy substrate 2. deposition of Ag electrode 3. the deposition of AsS_2 chalcogenide layer 4. photo diffusion and photo dissolution process induced by mercury lamp 5. filament formation under bias from conductive AFM.

Cross bar geometry: 1. Clean SiO_2 glassy substrate 2. deposition of W electrode 3. deposition of $GeSe_2$ chalcogenide layers 3. deposition of Ag layer 4. photo doping and photo dissolution induced by UV lamp 5. deposition of top Ag electrode 6. filament formation under bias.

Via-hole geometry: 1. Clean Si wafer 2. deposition of Pt layer 3. deposition of SiO_2 4. etching of SiO_2 5. deposition of $GeSe_2$ chalcogenide layer 6. deposition of Ag and filament formation.

9   Publications and conferences

B. Zhang, M. Fraenkl, J.M. Macak, T. Wagner, Ag filament and surface particle formation in Ag doped AsS_2 thin film, Mater. Lett. 163 (2016) 4–7.doi:10.1016/j.matlet.2015.08.131.

B. Zhang, P. Kutalek, P. Knotek, L. Hromadko, J.M. Macak, T. Wagner, Investigation of the resistive switching in Ag_xAsS_2 layer by conductive AFM, Appl. Surf. Sci. 382 (2016) 336–340. doi:10.1016/j.apsusc.2016.04.152.

R.M. Mawale, M. Alberti, B. Zhang, F. Max, T. Wagner, J. Havel, Structural elucidation of AgAsS2 glass by the analysis of clusters formed during laser desorption ionisation applying quadrupole ion trap time of flight mass spectrometry, Rapid Commun. Mass Spectrom. 30 (2016) 594–602. doi: 10.1002/rcm.7479.

T. Wagner, B. Zhang, S. Valkova, M. Fraenkl, M. Krbal, M. Frumar, G. Chen, Nanoscale memories in Chalcogenide Glass Films, Society Glass Technology Annual Meeting (Glass Reflections- Glass in the Year of Light), 7 - 9 September 2015, Cambridge, UK. Invited lecture.

T. Wagner, B. Zhang, S. Valkova, M. Fraenkl, M. Krbal, M. Frumar, G. Chen, Chalcogenide glass films for Nanoscale memories, 20th Int. Conf. ISNOG 2016, Niznij Novgorod, Russian, 21-26. Augest 2016.

B. Zhang, J. Kolar, J. M. Macak, T. Wagner, "Resistive switching of memory cells based on chalcogenides and nanoporous aluminum oxide'' International Days of Materials Science (IDMS) 2014, Pardubice, 12/2/2014.

B. Zhang, J. Kolar, J. M. Macak, T. Wagner, "Stages in resistive switching of memory cells based on chalcogenides and nanoporous AAO'' 66th Congress of Chemical Societies (7 - 10 September, Ostrava).

T. Wagner, B. Zhang, S. Valkova, M. Fraenkl, M. Krbal, M. Frumar, G. Chen, Ionic conductive chalcogenide films for nanoscale memories. 12th International Conference "Solid State Chemistry 2016", 18-23 September 2016, Prague. Book of abstracts, ISBN 978-80-7080-969-3.

B. Zhang, P. Kutalek, P. Knotek, L. Hromadko, J. M. Macak, T. Wagner, Investigation of the resistive switching in Ag_xAsS_2 layer by conductive AFM. 12th International Conference "Solid State Chemistry 2016", 18-23 September 2016, Prague. Book of abstracts, ISBN 978-80-7080-969-3.